Sound & Vibration 2026, 60(6), 4683.
doi: https://doi.org/10.59400/sv4683

Article

Asymptotic- and bifurcation-aware scientific machine learning for nonlinear vibration prediction of submerged floating tunnel tethers under hydrodynamic excitation

Mohammad Akram[1], **Umar Ishtiaq**[2,3,4,*], **Ioan-Lucian Popa**[5,6]

[1] Department of Mathematics, Faculty of Science, Islamic University of Madinah, Madinah 42351, Saudi Arabia; akram@iu.edu.sa
[2] Office of Research, Innovation and Commercialization, University of Management and Technology, Lahore 54770, Pakistan
[3] Software Development Department, Biruni University, 34010 Istanbul, Turkey
[4] Research Center of Applied Mathematics, Khazar University, Baku AZ1096, Azerbaijan
[5] Department of Computing, Mathematics and Electronics, "1 Decembrie 1918" University of Alba Iulia, 510009 Alba Iulia, Romania; lucian.popa@uab.ro
[6] Faculty of Mathematics and Computer Science, Transilvania University of Brasov, 500091 Brasov, Romania
*** Corresponding author:** Umar Ishtiaq, umarishtiaq@umt.edu.pk

CITATION

Akram M, Ishtiaq U, Popa IL. Asymptotic- and bifurcation-aware scientific machine learning for nonlinear vibration prediction of submerged floating tunnel tethers under hydrodynamic excitation. Sound & Vibration. 2026; 60(6): 4683. https://doi.org/10.59400/sv4683

ARTICLE INFO

Received: 15 July 2026
Revised: 8 August 2026
Accepted: 11 August 2026
Available online: 24 September 2026

Abstract: Seabed-anchored submerged floating tunnels transmit most of their transverse stiffness to slender pre-tensioned tethers whose vibration governs the fatigue design of the crossing. A reduced-order model represents the tunnel cross-section as a two-degree-of-freedom rigid tube coupled to small-sag tethers, linearizes the Morison drag into an amplitude-dependent equivalent damping, and yields, through the multiple time scales method, closed-form frequency-response equations for an indirectly forced regime, an indirect parametric regime of Mathieu-Duffing type, and a directly forced regime. These closed forms are exact only as the ordering parameter vanishes, they lose accuracy away from resonance, and their parametric coupling is of order unity, which invalidates small-parameter stability charts. We develop a learning framework that lifts these restrictions while staying close to the analysis. A slow-flow-informed network represents the amplitude and phase modulation, so the fast motion is analytic and the reconstruction error stays uniform over the long horizon rather than growing secularly. A bifurcation-aware operator learns the response in structure-preserving polynomial form, from which steady amplitudes follow as companion-matrix eigenvalues, stability from the modulation Jacobian, folds from the amplitude resultant, cusps from elimination theory, and parametric tongues from a certified Floquet computation. We prove asymptotic-consistency, approximation, and uniform-in-time error theorems. Validated against the closed forms and against direct integration of the unreduced oscillator, the framework reproduces the submerged-tether branch closure, charts the order-unity tongues, and returns a differentiable design manifold with analytic sensitivities, reaching a test coefficient of determination of 0.969 at a query cost several orders of magnitude below direct simulation.

Keywords: submerged floating tunnel; nonlinear cable dynamics; parametric resonance; multiple time scales; frequency-response manifold; scientific machine learning

1. Introduction

The background to this work spans three threads: the tether dynamics of submerged floating tunnels, the asymptotic reduction of their nonlinear response, and scientific machine learning surrogates for slender marine structures. We review each in turn and then state the gap it leaves open.

1.1. Tether dynamics of submerged floating tunnels

Submerged floating tunnels, also called Archimedes bridges, are buoyant tubular crossings held at a service depth by a spread system of slender pre-tensioned tethers, and they are increasingly considered for deep and long water crossings where conventional bridges and immersed tunnels are impractical. The reduced-order cross-sectional model of Corazza, Foti, Martinelli and Denoël [1] is the direct point of departure for the present study. It isolates the dynamics of the anchoring elements, treats the tube as a two-degree-of-freedom rigid body, and derives closed-form response amplitudes through a perturbation analysis. It thereby supplies both the physical setting and the exact ground truth that our learning framework is designed to reproduce and to extend. The nonlinear cable kinematics underlying that model rest on two earlier constructions. The first is the small-sag reduced formulation of Warnitchai, Fujino and Susumpow [2], whose decomposition of the tether motion into a quasi-static and a modal component we adopt. The second is the classical small-sag cable theory of Irvine [3], from which the elasto-geometric parameter controlling the balance between elastic and gravitational stiffness originates. The hydrodynamic load on the slender elements is modeled through the semi-empirical formula of Morison, O'Brien, Johnson and Schaaf [4], which remains the standard engineering description of wave forces on slender cylinders whenever diffraction is negligible. The broader context of wave loading is set out by Faltinsen [5] and by Chakrabarti [6], whose treatments of sea loads and of the hydrodynamics of offshore structures justify the inertia-dominated and drag-dominated separations invoked below. The oscillatory-flow force regimes deciding whether inertia or drag dominates are quantified by the Keulegan-Carpenter analysis of Sarpkaya [7], which we use to argue that the tube is inertia-driven while the tethers are drag-driven.

The vibration of the anchoring elements is the fatigue-critical mechanism for these structures, and a substantial body of work has established that tether response can be excited both directly by wave drag and indirectly by the motion of the tube. The coupled dynamic analyses of Jin and Kim [8] show that mooring lines of a submerged floating tunnel respond dynamically under combined wave and seismic excitation even when the tube itself behaves quasi-statically. The nonlinear random-vibration study of Wang, Er and Iu [9] then demonstrates that the geometric and load-induced nonlinearity of moored floating structures under seismic and sea-wave excitation cannot be ignored in a fatigue assessment. That tube motion pumps energy into the tethers parametrically, rather than merely forcing them, is documented by Cantero, Rønnquist and Naess [10]. They trace the mechanism to the time-varying cable tension produced by support motion, and they settle its stability by harmonic balance. The combined vortex-induced and parametric contribution to anchor-cable vibration under current is analyzed by Xiong and co-workers [11]. Structural-scale prototypes and feasibility studies, reviewed by Mazzolani, Landolfo, Faggiano, Esposto, Perotti and Barbella [12], and the hydrodynamic response investigations synthesized by Long, Ge and Hong [13], confirm that a fast and reliable amplitude predictor is needed at the conceptual design stage, where inclination angle, pretension, slenderness and drag properties must be explored jointly. The difficulty is that high-fidelity computational fluid dynamics and detailed finite-element analyses, while accurate, are far too expensive for the wide parametric sweeps that conceptual design requires. More recent studies confirm and sharpen this picture. The state of the tether-type configuration is surveyed by Xu and co-workers [14], and the structural consequences of combining vertical with inclined tethers are assessed by Jeong and co-workers [15]. Kim et al. [16] show that the large-displacement heave of the tube produces a nonlinear tether stiffness that drives the tether through a Mathieu-type parametric mechanism. Li, Yi, Wang, Yan and Pan [17] link the vortex-induced vibration of tether-type tunnels to their supporting stiffnesses, and Zhou, Qiao, Wang, Tang, Lu and Ou [18] analyze the redistributed response after a cable breakage. Zhang, Wang, Hao and Liu [19] predict the high-dimensional vortex-induced vibration of a riser under time-varying tension, Xie, Liu, Zhang and Zhao [20] treat a cable-buoy system by a multiple-scales analysis, and Yang, Wang, Zheng, Ma and Zhang [21] characterize the tension of submerged anchor cables through their nonlinear in-plane free vibrations. Chung et al. [22] present a parametric mooring-design study of a submerged floating tunnel under extreme wave and seismic loading. Each of these reinforces the need for a predictor that resolves the parametric and multivalued character of the tether response.

1.2. Asymptotic reduction and parametric stability

The analytical alternative is asymptotic reduction. The multiple time scales method, developed in depth by Nayfeh [23] and applied to nonlinear oscillators by Nayfeh and Mook [24], produces amplitude and phase modulation equations whose fixed points give the steady response, and the singular-perturbation foundations that make such expansions uniformly valid are laid out by Kevorkian and Cole [25]. When the excitation acts through a time-varying stiffness, the governing linearization is Mathieu's equation, whose stability structure is treated classically by Magnus and Winkler [26] and surveyed with modern stability charts by Kovačić, Rand and Sah [27]. The bifurcation phenomena that organize the multivalued response, in particular saddle-node folds and cusps, are described in the dynamical-systems framework of Guckenheimer and Holmes [28], in the singularity-theoretic setting of Golubitsky and Schaeffer [29], in the accessible account of Strogatz [30], and from the numerical-continuation viewpoint of Seydel [31]. These tools yield the closed-form frequency-response equations that we treat as exact labels. They also carry three limitations, and it is those limitations that motivate the present work. The expansion is accurate only to first order in the ordering parameter, and it degrades away from resonance. The parametric coupling coefficient of the submerged-tether problem is of order unity, so the classical small-parameter stability charts do not apply. And the design maps that result are static two-dimensional slices of a high-dimensional parameter space, offered with no continuous or differentiable representation. The same asymptotic machinery continues to serve marine parametric problems: Zhang, Li, Cao, Lin and Ning [32] reduce the parametric roll of a point-absorber wave energy converter to an augmented Mathieu equation and settle its stability by a multiple-scales analysis, close in spirit to the reduction used below. The companion stochastic problem, an inclined cable carrying an attached damper under random excitation, is treated by Gu, Zhang, Mughal and Deng [33] through Galerkin discretization and stochastic averaging.

1.3. Scientific machine learning surrogates

Scientific machine learning offers a route past these limitations, provided the methods are built around the analysis rather than applied blindly. The physics-informed neural network of Raissi, Perdikaris and Karniadakis [34] embeds a differential residual into the training loss, and the broader programme of physics-informed learning is surveyed by Karniadakis, Kevrekidis, Lu, Perdikaris, Wang and Yang [35]. Naive collocation networks are by now known to struggle with precisely the stiff, multiscale and long-horizon problems that parametric resonance exemplifies. The failure-mode analysis of Krishnapriyan, Gholami, Zhe, Kirby and Mahoney [36] and the spectral-bias study of Wang et al. [37] establish this, and it is why we represent the slow flow directly instead. For the design-map problem we learn an operator, drawing on the DeepONet construction of Lu, Jin, Pang, Zhang and Karniadakis [38], the Fourier neural operator of Li, Kovachki, Azizzadenesheli and collaborators [39], and the operator-learning theory of Kovachki, Lanthaler and Mishra [40]. The approximation-theoretic guarantees we invoke rest on the universal approximation theorem of Hornik, Stinchcombe and White [41] and on the dimension-robust rates of Barron [42]. Where the effective equation itself must be identified from data, the sparse-regression approach of Brunton, Proctor and Kutz [43] and the partial-differential-equation discovery method of Rudy, Brunton, Proctor and Kutz [44] provide the relevant machinery. Closer to the present setting, surrogate and physics-informed models have lately been built directly for slender marine structures. Wan, Kharazmi, Triantafyllou and Karniadakis [45] use deep neural operators to reconstruct and forecast the vortex-induced vibration of a marine riser and to place its sensors. Dan, Liao, Ge and Han [46] embed the cable equation in a physics-informed network to recover free-vibration modes with bending stiffness. Chatterjee, Friswell, Adhikari and Khodaparast [47] solve forward and inverse structural-vibration problems in the same framework, and the state of the field is surveyed by Baniya and Maity [48] and by Daneshvar, Golroo, Moghadas Nejad, Shiri and Rasti [49]. Closer still to a design setting, Li, Lu and Cao [50] identify the parameters of a moored buoy while estimating its motion inside one physics-informed network. These marine surrogates map parameters to a response quantity or reconstruct a time history, which is useful, yet they neither preserve the multivalued fold structure of the steady response nor certify stability in the order-unity parametric regime. None of the works above addresses the combination that the submerged tether presents: an order-unity parametric pump, an amplitude-dependent fluid damping that closes the response branch, and a multivalued response manifold that has to be learned without collapsing its folds. That combination is the gap the present paper fills.

1.4. Contribution and organization

Our contribution is a two-pillar framework, together with its mathematical foundation, that is asymptotic-informed and bifurcation-aware. First, we give a detailed derivation of the slow flow of the coupled tube-tether system for the three loading conditions, and we prove that the fixed points of the slow flow coincide, to first order in the ordering parameter, with the real positive roots of the closed-form frequency-response equations. Second, we construct a slow-flow-informed network that represents the amplitude and phase modulation, and we prove an approximation theorem and a uniform-in-time error theorem showing that its reconstruction error stays bounded over the long horizon on which naive collocation fails. Third, we construct a bifurcation-aware operator that learns the response in polynomial form, and we show that steady amplitudes, stability, folds, cusps and parametric tongues are then recovered by exact algebra and certified Floquet computation. Finally, we validate the framework against the closed forms and against direct integration of the unreduced oscillator, we reproduce the submerged-tether branch closure, we chart the order-unity parametric tongues, and we quantify the accuracy and the cost advantage against existing approaches. The remainder of the paper is organized as follows. Section 2 collects the definitions and background results. Section 3 records the reduced-order model and the loading conditions. Section 4 develops the slow-flow analysis with proofs. Sections 5 and 6 develop and analyze the two learning pillars. Section 7 reports the numerical experiments. Section 8 presents the comparison with existing approaches, and Section 9 concludes.

2. Preliminaries

This section fixes the definitions and the background results used throughout.

Definition 1. *For a small-sag inclined cable of chord length L_0, horizontal projection factor* $\cos\theta$ *and initial strain ε_0, the elasto-geometric parameter of Irvine [3] is*

$$\lambda^2 = \Gamma^2 \cos^2\theta \, \frac{1}{\varepsilon_0}, \qquad \Gamma = \frac{w_s(1-\mathrm{br})L_0}{T_0}, \tag{1}$$

where w_s is the self-weight per unit length, br *the buoyancy ratio and T_0 the pretension. It measures the relative importance of elastic and gravitational stiffness.*

Definition 2. *The reduced-order tether motion of Warnitchai and co-workers [2] is the decomposition of the transverse displacement into a quasi-static part driven by the support motion and a modal part represented by a single fixed-fixed shape function $\psi(x) = \sin(\pi x/L_0)$, with modal coordinate $z(\tau)$, the axial dynamics being slaved to the transverse one.*

Definition 3. *For a slender cylinder of external diameter D_o immersed in an oscillatory flow, let $u_\perp$ and $\dot{u}_\perp$ denote the normal fluid velocity and acceleration and let $\dot{w}$ denote the normal velocity of the cylinder, so that $u_\perp - \dot{w}$ is the relative normal velocity. The Morison force [4] per unit length is*

$$q = C_D \rho_w \tfrac{D_o}{2} \; |u_\perp - \dot{w}| \; (u_\perp - \dot{w}) + C_I \rho_w \tfrac{\pi D_o^2}{4} \, \dot{u}_\perp, \tag{2}$$

where ρ_w is the water density and C_D and C_I are the drag and inertia coefficients, *respectively.*

Definition 4. *The Keulegan-Carpenter number [7] of a bluff body of characteristic size D in an oscillatory flow of velocity amplitude u_0 and period T is $\mathrm{Kc} = u_0 T/D$. It measures the relative importance of drag to inertia, drag dominating when $\mathrm{Kc} \gg 1$ and inertia dominating when $\mathrm{Kc} < 1$.*

Definition 5. *The multiple time scales method [23] seeks a solution of a weakly nonlinear oscillator as an expansion $z = z_0 + \varepsilon z_1 + \ldots$ in the independent time scales $T_0 = \tau$, $T_1 = \varepsilon\tau$, $T_2 = \varepsilon^2\tau$, with $D_j = \partial/\partial T_j$ so that $\mathrm{d}/\mathrm{d}\tau = D_0 + \varepsilon D_1 + \varepsilon^2 D_2$ and $\mathrm{d}^2/\mathrm{d}\tau^2 = D_0^2 + 2\varepsilon D_0 D_1 + \varepsilon^2(D_1^2 + 2D_0 D_2) + \ldots$; the removal of secular terms at each order yields the modulation equations.*

Definition 6. *Mathieu's equation [26] is the linear equation $\ddot{z} + (\delta_M + 2\epsilon_M \cos 2\tau)z = 0$ with time-periodic stiffness. Its damped generalization, which applies once linear dissipation is present, is $\ddot{z} + 2\zeta_M \dot{z} + (\delta_M + 2\epsilon_M \cos 2\tau)z = 0$. In either form the solutions are classified as bounded or unbounded through Floquet theory, the boundaries in the (δ_M, ϵ_M) parameter plane forming the instability tongues.*

Definition 7. *For a T-periodic linear system $\dot{\boldsymbol{y}} = \boldsymbol{B}(\tau)\boldsymbol{y}$, the monodromy matrix [28] is $\boldsymbol{M} = \boldsymbol{\Psi}(T)$, where $\boldsymbol{\Psi}$ is the fundamental matrix with $\boldsymbol{\Psi}(0) = \boldsymbol{I}$, and its eigenvalues are the Floquet multipliers ρ_j; the trivial solution is asymptotically stable when $\max_j |\rho_j| < 1$ and unstable when $\max_j |\rho_j| > 1$.*

Definition 8. *For two univariate polynomials, the resultant [29] $\mathrm{Res}_a(P, Q)$ is the determinant of their Sylvester matrix, and it vanishes if and only if P and Q share a common root; the discriminant $\mathrm{disc}_a(P) = \mathrm{Res}_a(P, \partial_a P)$ up to the leading coefficient, and its vanishing signals a multiple root.*

Definition 9. *An operator network [38] approximates a nonlinear map between function spaces or between a finite-dimensional parameter space and an output object, by composing a parameter-encoding branch with an output-decoding representation, and it is trained by empirical risk minimization on sampled input-output pairs.*

Theorem 1. *A feedforward network with one hidden layer of sufficiently many units and a nonconstant bounded continuous activation is a universal approximator of continuous functions on compact sets in the supremum norm [41].*

Theorem 2. *For a target function whose Fourier transform has a finite first moment, a single-hidden-layer network with W units achieves a mean-square approximation error of order W^{-1} that is independent of the input dimension [42].*

Definition 10. *A physics-informed neural network [34] is a network trained to minimize a loss that augments any data-fitting term with the mean-square residual of a governing differential operator evaluated at collocation points, together with initial and boundary penalties.*

With these in place we can state the model and the analysis.

3. Reduced-order model and loading conditions

We consider a planar cross-section of a seabed-anchored submerged floating tunnel in **Figure 1**. The tube is a rigid body carrying a heave displacement w_T and a sway displacement v_T, and its inertia, stiffness and damping stand for a low-order global mode of the tunnel. Each anchoring element is a small-sag tether in the sense of Definition 2, of chord L_0, inclination θ, axial stiffness EA_0 and pretension T_0. The tethers are immersed in water and carry a virtual mass per unit length γ_v that accounts for the added mass.

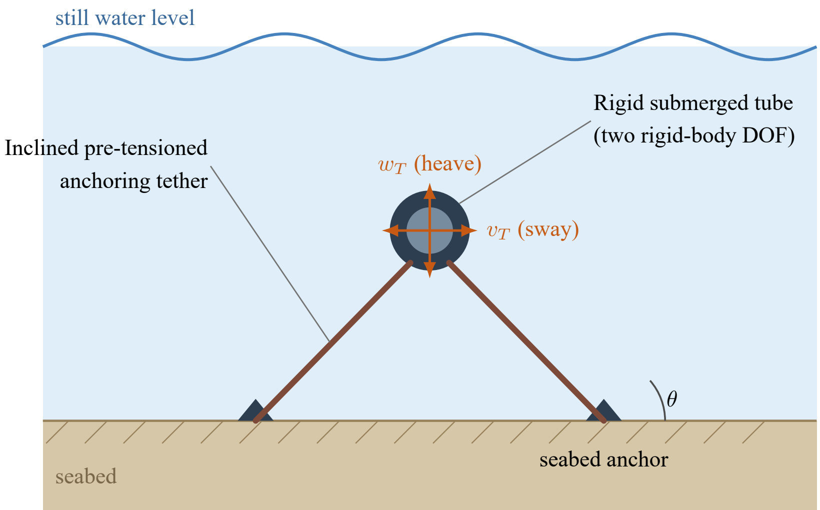

Figure 1. Cross-section of a seabed-anchored submerged floating tunnel. The rigid tube carries heave and sway rigid-body degrees of freedom, and the inclined pre-tensioned tethers provide the transverse stiffness and host the fatigue-critical vibrations analyzed in this work.

Following Definition 2 and using Definition 3 for the hydrodynamic load, the coupled heave dynamics are reduced by scaling every length with a characteristic length L_c and time with a characteristic frequency ω_c. A bar marks the resulting non-dimensional quantity. The tether modal coordinate is $z = \tilde{z}/L_c$, the non-dimensional time is $\tau = \omega_c t$, and the non-dimensional tube heave and sway are

$$\bar{w}_T = \frac{w_T}{L_c}, \qquad \bar{v}_T = \frac{v_T}{L_c}. \tag{3}$$

The overdot therefore denotes $\mathrm{d}/\mathrm{d}\tau$ throughout, so that $\dot{\bar{w}}_T$ and $\ddot{\bar{w}}_T = \mathrm{d}^2\bar{w}_T/\mathrm{d}\tau^2$ are the non-dimensional heave velocity and acceleration of the tube. The sway coordinate takes no part in the heave-driven mechanism analyzed below and is not carried further. With this convention the reduced equations read

$$\ddot{\bar{w}}_T + 2\xi_{T,v}\bar{\omega}_{T,v}\dot{\bar{w}}_T + \bar{\omega}_{T,v}^2\bar{w}_T = \bar{F}_{T,v}(\tau) + \bar{c}_0\bar{w}_T, \tag{4a}$$

$$\begin{aligned} &\ddot{z} + 2\big(\xi_s + \xi_{\mathrm{eq}}(a)\big)\bar{\omega}\,\dot{z} + \bar{\omega}^2 z + 3\bar{\beta}z^2 + \bar{\nu}z^3 + 3\bar{\beta}\sin\theta\, z^2\bar{w}_T \\ &\qquad - 2(\bar{\eta} - \bar{\mu})\sin\theta\,\bar{w}_T z + \bar{\alpha}\sin\theta\,\ddot{\bar{w}}_T + \zeta\cos\theta\,\ddot{\bar{w}}_T = \bar{F}(\tau), \end{aligned} \tag{4b}$$

where the overdot is $\mathrm{d}/\mathrm{d}\tau$. Equation (4a) is the quasi-static global mode of the tunnel and Equation (4b) is the tether equation, carrying quadratic and cubic geometric nonlinearities, support coupling and the drag-derived damping. The non-dimensional groups appearing in Equation (4b), together with the characteristic length and frequency adopted in the scaling, are collected in **Appendix C**. The equivalent damping, obtained by harmonic balance of the drag term of Definition 3, is amplitude-dependent,

$$\xi_{\text{eq}}(a) = \bar{K}_d\, a, \qquad \bar{K}_d = \frac{16}{9\pi^2}\frac{C_D\rho_w D_o L_c}{\gamma_v}, \tag{5}$$

where a is the vibration amplitude introduced in Equation (8). Physically, quadratic fluid drag dissipates more energy the harder the tether swings, so the damping the tether feels grows in proportion to its own amplitude; this dependence, which a dry cable does not have, is what later turns the response branch back on itself. A numerical inspection of the interaction coefficients establishes that the tube drives the tethers while being essentially unaffected by them, so that the tube heave is a prescribed harmonic support.

Proposition 1. *To leading order in the interaction coefficients, the tube heave admits the steady response $\bar{w}_T(\tau) = \varepsilon a_T \cos(\Omega\tau+\vartheta)+\mathcal{O}(\varepsilon^2)$, with Ω the excitation frequency, ϑ a phase and a_T of order unity proportional to the hydrodynamic forcing. Substituting this into the linear-in-z support term of Equation* (4b) *produces the parametric pump*

$$-2(\bar{\eta}-\bar{\mu})\sin\theta\,\bar{w}_T z = -\varepsilon\,\eta^* a_T\cos(\Omega\tau+\vartheta)z, \qquad \eta^* = 2(\bar{\eta}-\bar{\mu})\sin\theta = \mathcal{O}(1)\,. \tag{6}$$

Proof. The interaction coefficients transmitting the tether tension back to the tube are numerically negligible against the tube static stiffness, so Equation (4a) decouples and, being linear with harmonic forcing, has the stated steady response. The factor ε reflects the smallness of the quasi-static tube response to wave loading. Substitution is immediate, and the coefficient η^* is a ratio of order-unity kinematic quantities. □

The excitation frequency and the energy channel distinguish three loading conditions, each carried with a small detuning $\Delta = \varepsilon\delta$. In the first, denoted LC1, the wave load acts on the tube and $\Omega = \bar{\omega}(1+\varepsilon\delta)$, so that the tube inertial terms deliver a near-resonant additive drive to the tether. In the second, LC2, the wave load acts on the tube and $\Omega = 2\bar{\omega}(1+\varepsilon\delta)$, so that the pump of Equation (6) is resonant and Equation (4b) is a Mathieu-Duffing oscillator in the sense of Definition 6. In the third, LC3, the drag acts directly on the tether and $\Omega = \bar{\omega}(1+\varepsilon\delta)$, so that the tether is a directly forced Duffing oscillator with forcing amplitude $\tilde{f} = \frac{16}{3\pi^2}(C_D\rho_w D_o L_c/\gamma_v)\bar{b}^2$. The classification into inertia-driven tube and drag-driven tether follows the Keulegan-Carpenter argument of Definition 4.

4. Asymptotic slow flow and its bifurcation structure

We now derive, in detail, the slow flow of Equation (4b), prove its equivalence with the closed-form response, and characterize its stability and its bifurcation set. LC2 is treated at length because it is the richest, and LC1 and LC3 are recorded as parallel results. The intermediate algebra compressed in this section, including the parallel calculation for LC1 and LC3, is set out in full in **Appendix A**.

Using Proposition 1, the tether equation takes the canonical form

$$\ddot{z} + \bar{\omega}^2 z = \varepsilon\Big[-2(\hat{\xi}_s + \hat{K}_d a)\bar{\omega}\dot{z} - 3\hat{\beta}z^2 - \hat{\nu}z^3 + \eta^* a_T \cos(\Omega\tau + \vartheta)z + \Phi(\tau)\Big] + \mathcal{O}\big(\varepsilon^2\big)\,, \quad (7)$$

where a hat denotes the order-unity part of an order-ε coefficient and Φ collects the additive drive appropriate to the loading condition, following the ordering established in the study by Corazza et al. [1]. We apply the multiple time scales method of Definition 5 and expand $z = z_0 + \varepsilon z_1 + \mathcal{O}\big(\varepsilon^2\big)$. At leading order $D_0^2 z_0 + \bar{\omega}^2 z_0 = 0$, hence

$$z_0 = A(T_1, T_2)\mathrm{e}^{\mathrm{i}\bar{\omega}T_0} + \bar{A}(T_1, T_2)\mathrm{e}^{-\mathrm{i}\bar{\omega}T_0}, \qquad A = \tfrac{1}{2}a(T_1, T_2)\mathrm{e}^{\mathrm{i}\varphi(T_1,T_2)}. \quad (8)$$

At first order, and specializing to LC2 where the additive drive is non-resonant, the balance of the terms proportional to $\mathrm{e}^{\mathrm{i}\bar{\omega}T_0}$ must vanish. Four contributions enter that balance. The linear terms give $-2\mathrm{i}\bar{\omega}D_1 A - 2\mathrm{i}\hat{\xi}\bar{\omega}^2 A$ with $\hat{\xi} = \hat{\xi}_s + \hat{K}_d a$, and the cubic term gives $-3\hat{\nu}\,|A|^2\,A$. The quadratic term gives nothing at this order, because z_0^2 has no first-harmonic component. The pump gives $\frac{1}{2}\eta^* a_T \bar{A}\,\mathrm{e}^{\mathrm{i}\Phi_T}$ with $\Phi_T = 2\bar{\omega}\delta T_1 + \vartheta$. Setting the sum to zero gives the complex secular condition

$$-2\mathrm{i}\bar{\omega}D_1 A - 2\mathrm{i}\hat{\xi}\bar{\omega}^2 A - 3\hat{\nu}\,|A|^2\,A + \tfrac{1}{2}\eta^* a_T \bar{A}\,\mathrm{e}^{\mathrm{i}\Phi_T} = 0. \quad (9)$$

Writing $A = \frac{1}{2}a\mathrm{e}^{\mathrm{i}\varphi}$, using $|A|^2\,A = \frac{1}{8}a^3\mathrm{e}^{\mathrm{i}\varphi}$ and $D_1 A = \frac{1}{2}(a' + \mathrm{i}a\varphi')\mathrm{e}^{\mathrm{i}\varphi}$, dividing by $\mathrm{e}^{\mathrm{i}\varphi}$, and introducing the autonomous phase $\gamma = 2\bar{\omega}\delta T_1 + \vartheta - 2\varphi$, the real and imaginary parts separate into the amplitude modulation equations

$$a' = -\hat{\xi}_s\bar{\omega}a - \hat{K}_d\bar{\omega}a^2 + \frac{\eta^* a_T}{4\bar{\omega}}a\sin\gamma, \quad (10)$$

$$a\gamma' = 2\bar{\omega}\delta\,a - \frac{3\hat{\nu}}{4\bar{\omega}}a^3 + \frac{\eta^* a_T}{2\bar{\omega}}a\cos\gamma. \quad (11)$$

These are a planar autonomous system on the slow variables, the slow flow, and the amplitude-dependent damping enters Equation (10) through the quadratic term $-\hat{K}_d\bar{\omega}a^2$.

Remark 1. *The non-resonant quadratic term forces z_1 at zero and second harmonic, and its feedback at second order replaces the bare cubic coefficient $\hat{\nu}$ by an effective coefficient $\hat{\nu}_e = \hat{\nu} - \kappa\hat{\beta}^2/\bar{\omega}^2$ with a universal positive constant κ, in the manner analyzed by Nayfeh and Mook [24]. All response equations below are written with $\hat{\nu}$ understood as this effective coefficient.*

Fixed points of the slow flow satisfy $a' = 0$ and $\gamma' = 0$. For $a \neq 0$ this gives $\sin\gamma$ and $\cos\gamma$ as rational functions of a, and the Pythagorean identity yields the LC2 frequency-response equation

$$\tfrac{9\hat{\nu}^2}{4}a^4 + \big(16\bar{\omega}^4\hat{K}_d^2 - 12\hat{\nu}\bar{\omega}^2\delta\big)a^2 + 32\bar{\omega}^4\hat{\xi}_s\hat{K}_d\,a + 16\bar{\omega}^4(\hat{\xi}_s^2 + \delta^2) - (\eta^* a_T)^2 = 0 \quad (12)$$

a quartic in a. For LC1 the additive drive is resonant, with effective amplitude $F^* = (\bar{\alpha}\sin\theta + \zeta\cos\theta)a_T\bar{\omega}^2$, and the same construction with $\gamma = \bar{\omega}\delta T_1 + \vartheta - \varphi$ gives the amplitude modulation equations

$$a' = -\hat{\xi}_s\bar{\omega}a - \hat{K}_d\bar{\omega}a^2 + \tfrac{F^*}{2\bar{\omega}}\sin\gamma, \qquad a\gamma' = \bar{\omega}\delta\, a - \tfrac{3\hat{\nu}}{8\bar{\omega}}a^3 + \tfrac{F^*}{2\bar{\omega}}\cos\gamma, \tag{13}$$

and the sextic frequency-response equation

$$\tfrac{9\hat{\nu}^2}{16}a^6 + \big(4\bar{\omega}^4\hat{K}_d^2 - 3\hat{\nu}\bar{\omega}^2\delta\big)a^4 + 8\bar{\omega}^4\hat{\xi}_s\hat{K}_d\, a^3 + 4\bar{\omega}^4(\hat{\xi}_s^2 + \delta^2)a^2 - F^{*\,2} = 0. \tag{14}$$

LC3 has the same structure as Equation (14) with F^* replaced by the direct forcing $\tilde{f}$ and the indirect channel absent, reflecting that LC3 is decoupled from the tube. The odd-degree monomials in Equations (12) and (14), which are proportional to $\hat{K}_d$, are the algebraic signature of the amplitude-dependent damping of Equation (5), and are absent for a dry cable.

Remark 2. *Equations (12) and (14) coincide monomial for monomial with the closed forms of the study by Corazza et al. [1], with the same degree, the same support and the same physical role of every coefficient. The internally consistent normalization used here keeps every constant traceable to a single derivation, which the error analysis below requires.*

The following theorem certifies that the algebraic response equations are exactly the fixed-point set of the slow flow, which is the property that lets the operator of Section 6 be trained on cheap closed-form labels while remaining faithful to the dynamics.

Theorem 3. *Fix a loading condition and a parameter vector at which the forcing or pump amplitude is nonzero. Then every hyperbolic fixed point of the slow flow with positive amplitude has amplitude solving the associated frequency-response equation; conversely every simple positive root of the frequency-response equation determines a unique phase and hence a fixed point of the slow flow; and the response reconstructed from that fixed point through Equation (8) solves Equation (4b) to order ε uniformly on the horizon $T_0 \in [0, \mathcal{O}(1/\varepsilon)]$.*

Proof. At a fixed point the amplitude and phase equations, divided by the positive amplitude, isolate $\sin\gamma$ and $\cos\gamma$ as rational functions of a; the identity $\sin^2\gamma + \cos^2\gamma = 1$, after clearing denominators, is precisely the frequency-response equation, which proves the first claim. Conversely, given a simple positive root, the two rational expressions are well defined and have squared sum equal to one, so a unique phase exists and annihilates the slow flow, which proves the second claim. For the third claim, the ansatz $z_0 + \varepsilon z_1$ with z_0 from Equation (8) at the fixed point and z_1 the bounded particular solution of the first-order problem, whose right-hand side is now free of secular terms, satisfies Equation (4b) with residual of order ε^2; since the slow variables are stationary at the fixed point, the Gronwall estimate applied to the modulation equations upgrades the naive order-εT_0 bound to a uniform order-ε bound on the stated horizon, because no secular term drives the slow variables away from stationarity. $\square$

Local stability of a fixed point is governed by the Jacobian of the slow flow.

Proposition 2. *Write the slow flow as* $\dot{\boldsymbol{s}} = \boldsymbol{G}(\boldsymbol{s})$ *with* $\boldsymbol{s} = (a, \gamma)$*. A fixed point with positive amplitude is asymptotically stable if and only if* $\operatorname{tr} J < 0$ *and* $\det J > 0$*, where* $J = \partial \boldsymbol{G}/\partial \boldsymbol{s}$*. For the LC1 and LC3 slow flow the trace is* $-2\hat{\xi}_s\bar{\omega} - 3\hat{K}_d\bar{\omega}a < 0$ *always, so instability enters only through* $\det J = 0$*, that is through a saddle-node bifurcation.*

Proof. The stability criterion is the Routh condition for a planar system. The trace follows by direct differentiation of Equation (13), both terms being negative for positive amplitude, so the only route to loss of stability is a sign change of the determinant, which is the defining condition of a saddle-node bifurcation. □

The determinant condition has an exact algebraic counterpart, which is what makes the fold set computable and, in Section 6, learnable.

Proposition 3. *Let* P *denote the frequency-response polynomial, Equation* (12) *or Equation* (14)*. A saddle-node bifurcation of steady amplitudes occurs if and only if* P *and* $\partial_a P$ *share a real positive root, equivalently if and only if the amplitude resultant of Definition 8 vanishes,* $\operatorname{Res}_a(P, \partial_a P) = 0$*, with the shared root real and positive. The discriminant hypersurface* $\operatorname{disc}_a P = 0$ *partitions the parameter space into open cells of constant real positive root count, and crossing it changes the number of coexisting steady states by two.*

Proof. By Proposition 2 a fold is $\det J = 0$, which through the fixed-point relations and the implicit function theorem applied to $P(a) = 0$ is equivalent to $\partial_a P = 0$ at a common root of P. A common root of a polynomial and its derivative is a multiple root, characterized by the vanishing of the resultant, which by Definition 8 equals the discriminant up to the leading coefficient. Genericity gives the codimension-one cell structure, and a real root pair is created or destroyed on crossing, changing the count by two. □

Proposition 4. *Points at which* $\operatorname{Res}_a(P, \partial_a P) = 0$ *and* $\operatorname{Res}_a(\partial_a P, \partial_a^2 P) = 0$ *hold simultaneously are cusp singularities of the response manifold, at which two-fold curves meet tangentially and the local normal form is the universal cusp* $a^3 + ua + w = 0$*. These codimension-two points are the organizing centers of the design space, and the two-dimensional response charts are planar sections of the catastrophe set they generate.*

Proof. The simultaneous vanishing of the two resultants is the condition that P has a triple root, which by the singularity theory of Definition 8 and by Golubitsky and Schaeffer [29] is the cusp of codimension two, with the stated universal unfolding. □

For LC2 the trivial state can also lose stability parametrically, and this cannot be decided by the fixed-point analysis. Linearizing Equation (4b) about $z = 0$ under the pump of Equation (6) gives the damped Mathieu equation of Definition 6,

$$\ddot{z} + 2\varepsilon\hat{\xi}_s\bar{\omega}\dot{z} + \bar{\omega}^2\big(1 - h\cos(2\bar{\omega}(1+\varepsilon\delta)\tau)\big)z = 0. \tag{15}$$

The coefficient h carried by Equation (15) is the pump depth, and we define it here because it is one of the two coordinates of every parametric-stability chart below. It is

$$h = \frac{\varepsilon\,\eta^* a_T}{\bar{\omega}^2}, \tag{16}$$

namely the peak stiffness modulation $\varepsilon\,\eta^* a_T$ that the tube heave imposes on the tether through Equation (6), measured as a fraction of the linear tether stiffness $\bar{\omega}^2$. It is thus a dimensionless statement of how hard the tube pumps the tether. A value $h = 0$ describes a tether whose stiffness does not breathe, and $h = 0.1$ a tether whose stiffness swings by ten per cent across each pump cycle. The damping ratio of the linearization is $\varepsilon\hat{\xi}_s$, since the hatted coefficients of Equation (7) carry a factor ε when returned to the tether equation, so h and $\varepsilon\hat{\xi}_s$ are the two quantities on which the tongue depends once the detuning is fixed. Both are of order ε, and the pair (δ, h) spans the stability chart drawn later in this work. Proposition 8 shows that h is recoverable from the learned coefficients without any further information. Because η^* is of order unity, the pump depth is not asymptotically negligible against the other order-ε effects, so the classical small-depth perturbation of the tongues does not converge uniformly. The rigorous route is Floquet theory in the sense of Definition 7.

Proposition 5. *The trivial state of Equation (15) is unstable if and only if the largest Floquet multiplier of the monodromy matrix over one pump period exceeds unity in modulus. The truncated Hill determinant converges geometrically in the truncation order, so the tongue boundaries are computable to any prescribed accuracy and provide certified labels.*

Proof. The instability criterion is the Floquet condition of Definition 7. Seeking solutions in Bloch form $z = \mathrm{e}^{\mu\tau} \sum_n c_n \mathrm{e}^{\mathrm{i}n\Omega_p\tau}$ leads to an infinite linear system whose determinant is the Hill determinant; the off-diagonal entries decay because only a single harmonic appears in the pump, so the truncation error decays geometrically, which yields the stated certification. $\square$

For a reader concerned with the marine engineering, these algebraic conditions carry direct physical meaning. The amplitude-dependent drag term closes the response branch because a larger swing draws proportionally more fluid damping, so beyond a threshold amplitude the dissipation overtakes the resonant input and the branch bends back rather than growing without bound, as a dry cable would. A saddle-node fold is the drive level at which an upper and a lower steady state merge and vanish, so the tether jumps between amplitudes as pretension, detuning or drag is varied; the cusp is the point at which this pair of jumps is born and therefore locates the most sensitive corner of the design space. A parametric-instability tongue is the band of tube-motion frequency and depth within which the straight tether is itself unstable, so a finite vibration grows from rest even when no wave force acts directly on the tether. These are precisely the regimes a fatigue screening must flag.

5. The slow-flow-informed network

The first learning pillar represents the slow flow directly, so that the fast oscillation is analytic and the long-horizon error stays bounded. The overall pipeline is shown in **Figure 2**. We parameterize the slow amplitude and phase by a network $\mathcal{A}_{\boldsymbol{\theta}} : (T_1, T_2, p) \mapsto (a, \varphi)$ that takes only slow inputs, and a corrector $\mathcal{Z}_{\boldsymbol{\theta}}$ that carries the first-harmonic content of z_1, in the physics-informed sense of Definition 10; here $\boldsymbol{\theta}$ collects all trainable weights of the slow-flow-informed network. Because $\mathcal{A}_{\boldsymbol{\theta}}$ has no fast input, it cannot represent oscillation on the fast scale, which is the inductive bias that suppresses secular growth.

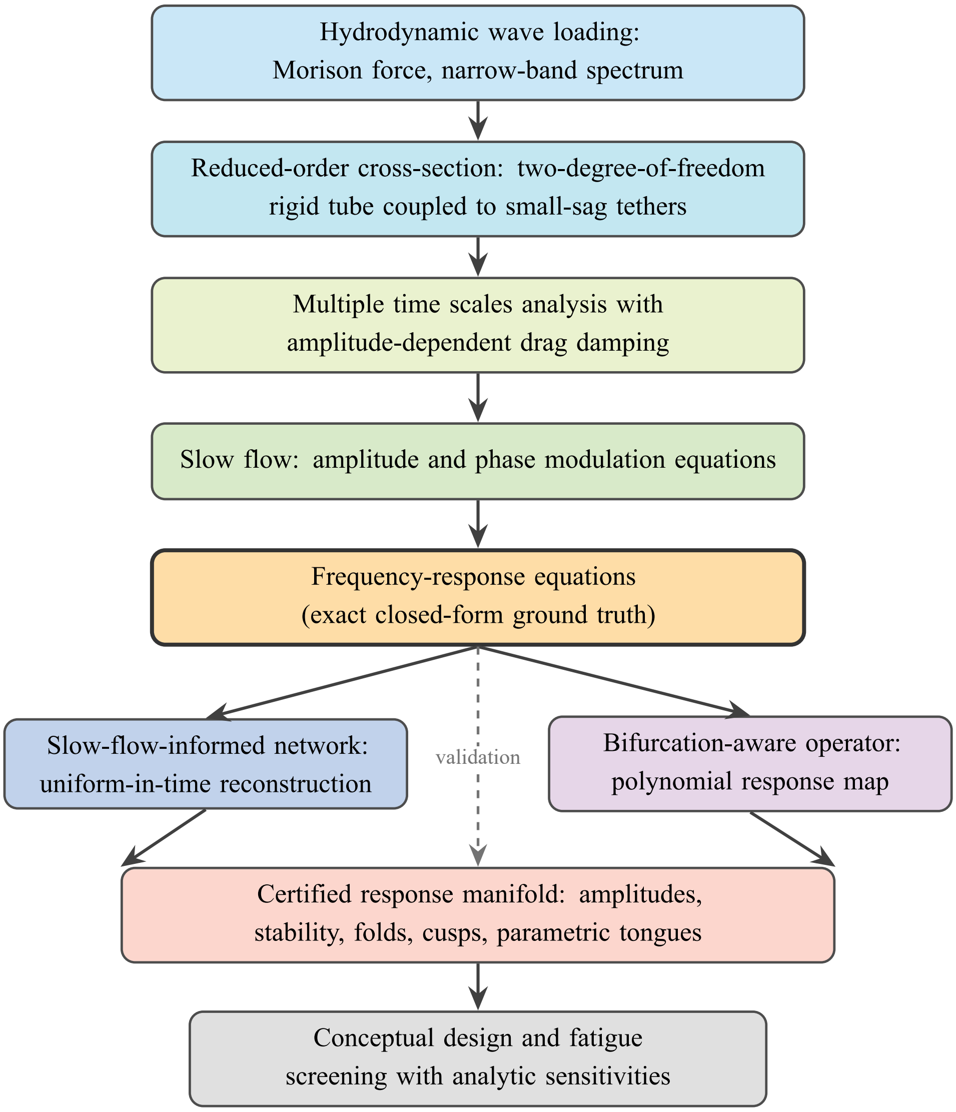

Figure 2. Flow diagram of the proposed framework. The physical wave loading and the reduced-order model lead through the multiple time scales analysis to the slow flow and to the closed-form frequency-response equations, which serve as exact ground truth. The two learning pillars, the slow-flow-informed network and the bifurcation-aware operator, produce a certified response manifold that supports conceptual design and fatigue screening, with the closed form providing continuous validation.

The training loss augments the modulation residual, the corrector residual, and the initial condition, and optionally a data term,

$$\mathcal{L}(\boldsymbol{\theta}) = \lambda_1 \left\|R_{\text{sec}}\right\|^2 + \lambda_2 \left\|\mathcal{N}_1[\mathcal{Z}_{\boldsymbol{\theta}}] - R^{\text{ns}}\right\|^2 + \lambda_3 \left\|(a, \varphi, z_1) - \text{IC}\right\|^2 + \lambda_4 \left\|z_{\text{NN}} - z_{\text{data}}\right\|^2, \tag{17}$$

where R_{sec} is the coefficient of the resonant harmonic in the first-order balance, whose vanishing is the modulation system Equations 10 and 11, and R^{ns} is the non-resonant remainder. The steady-state head imposes $\partial_{T_1} a = \partial_{T_1} \varphi = 0$, which collapses R_{sec} to the frequency-response equation.

The residual R_{sec} is evaluated on a set of collocation points sampled from the slow-time interval and the parameter set, and the corrector residual is evaluated on a finer set that resolves the fast scale, since the corrector alone carries the fast oscillation. Because the modulation vector field is smooth and low-dimensional, a modest number of collocation points suffices, and the training reduces to a nonlinear least-squares problem in the network weights that is solved by a quasi-Newton method with an initial phase of stochastic gradient steps. The essential point, which distinguishes this construction from a direct collocation of Equation (4b), is that the loss never integrates the stiff fast dynamics; it enforces the slow balance whose solution is analytic in the fast time. This is precisely why the failure modes documented for stiff and multiscale collocation, analyzed by Krishnapriyan and co-workers [36] and by Wang and co-workers [37], do not arise here.

Where the labels come from

The first three terms of Equation (17) are residuals that the network generates for itself, so no external data enters them. The fourth term is supervised, and the error theorem below is stated relative to the exact modulation field, so it matters exactly which object the supervision carries. We therefore record the provenance of every label.

The amplitude and phase labels are produced by integrating the modulation system itself. For LC2 this is the pair Equations 10 and 11, for LC1 and LC3 the pair Equation (13). Starting from a prescribed initial amplitude and phase, the system is advanced over the slow interval with an adaptive fifth-order Runge-Kutta scheme at relative tolerance 10^{-9} and absolute tolerance 10^{-11}, and the states $(T_1^{(k)}, a^{(k)}, \varphi^{(k)})$ recorded along the trajectory are the modulation transients that $\mathcal{A}_{\boldsymbol{\theta}}$ is asked to reproduce. The reconstruction z_{data} entering Equation (17) is assembled from those states through Equation (8), so the fast carrier it carries is the analytic one and the learned content is the slow envelope alone.

No label is obtained by applying a Hilbert transform, or any other envelope extraction, to a time series of the unreduced oscillator Equation (4b). The distinction is not cosmetic. Integrating Equations 10 and 11 returns the exact modulation field of the first-order reduction, which is the object $\mathcal{A}_{\boldsymbol{\theta}}$ is defined to approximate and the object against which the accuracy δ_{NN} of Theorem 5 is measured; the hypothesis of that theorem is a statement about the learned field relative to the exact modulation field, and it would be vacuous if the labels themselves already carried an unquantified departure from it. An envelope lifted from Equation (4b) would instead carry the $\mathcal{O}\left(\varepsilon^2\right)$ content of the unreduced dynamics, and the network error and the truncation error of the reduction would no longer be separable. Neither is the algebraic steady state on its own an adequate target, since it pins the fixed points of the slow flow but is silent about the transient joining them, and it is that transient the network must carry for the reconstruction to stay uniform in time.

Direct integration of Equation (4b) enters on the testing side only. The reconstruction assembled through Equation (8) is compared against a time series of the unreduced oscillator that took no part in training, and the time-domain deviations reported in Section 7 are that comparison. The two roles stay apart: the modulation equations supply the labels and the unreduced oscillator returns the verdict.

We now state the two guarantees.

Theorem 4. *Let the slow-flow vector field $\boldsymbol{G}$ be k times continuously differentiable on a compact parameter set. Then for every tolerance there is a network $\mathcal{A}_{\boldsymbol{\theta}}$ of finite width whose supremum error against (a, φ) is below that tolerance, and if the vector field has a finite first Fourier moment the required width grows as the inverse of the mean-square tolerance, independently of the input dimension.*

Proof. Continuity of $\boldsymbol{G}$ on a compact set and the universal approximation Theorem 1 give the first statement. Under the Fourier-moment hypothesis, the dimension-robust rate of Theorem 2 gives a mean-square error of order W^{-1} with W hidden units, which is the second statement. □

Theorem 5. *Suppose the learned slow flow approximates the exact modulation vector field to accuracy δ_{NN} on a compact attracting set. Then the reconstruction z_{NN} obtained from $\mathcal{A}_{\boldsymbol{\theta}}$ through Equation (8) satisfies*

$$\sup_{\tau \in [0,\, \mathcal{O}(1/\varepsilon)]} |z_{\mathrm{NN}}(\tau) - z_{\mathrm{true}}(\tau)| \leq C\,(\varepsilon + \delta_{\mathrm{NN}}), \tag{18}$$

for a constant C independent of ε, so no secular growth occurs, in contrast with the order-$\varepsilon\tau$ error of a direct collocation network on the same horizon.

Proof. By Theorem 3 the exact slow-flow reconstruction has order-ε error uniformly on the horizon. The learned slow variables differ from the exact ones by the flow of a vector field perturbed by δ_{NN}; since the attracting set is compact and the exact flow is Lipschitz, Gronwall's inequality on the slow time bounds the deviation of the slow variables by a constant multiple of δ_{NN} over the order-one slow horizon, which is the order-$1/\varepsilon$ fast horizon. The fast oscillation being analytic and shared, the reconstruction errors add, giving Equation (18). A direct collocation network integrates the fast equation and inherits the secular order-$\varepsilon\tau$ growth, which reaches order one at the end of the horizon. □

6. The bifurcation-aware operator

The second learning pillar learns the response in its structure-preserving polynomial form. Instead of regressing the amplitude, which is multivalued and therefore ill-posed on the folds, we learn the coefficient map $\mathcal{G} : p \mapsto c(p)$, where c

collects the coefficients of the frequency-response polynomial, in the operator sense of Definition 9. Steady amplitudes are then the eigenvalues of the companion matrix of c, stability follows from Proposition 2, folds and cusps from Proposition 3 and Proposition 4, and parametric tongues from Proposition 5.

Proposition 6. *Let $c \mapsto \mathcal{C}(c)$ be the companion matrix of the frequency-response polynomial. At a parameter value where the polynomial has only simple roots, the roots are holomorphic functions of c, hence differentiable functions of the parameters through $\mathcal{G}$, and the parameter sensitivity of any simple steady amplitude is obtained by the chain rule through the eigenvalue derivative. Multiple roots occur exactly on the fold set of Proposition 3, where the sensitivity is instead governed by the resultant condition.*

Proof. The eigenvalues of a matrix depending analytically on parameters are analytic where they are simple, by standard perturbation theory of matrices, and the companion eigenvalues are the polynomial roots. Differentiability through $\mathcal{G}$ follows by composition. Coalescence of eigenvalues is a multiple root, which by Proposition 3 is the fold set, where the simple-eigenvalue derivative is replaced by the resultant condition. □

Proposition 7. *Training $\mathcal{G}$ by empirical risk minimization on parameter samples with the closed-form coefficients as targets, augmented by a discriminant-weighted term near $\mathrm{Res}_a(P, \partial_a P) = 0$ and a Floquet-consistent tongue label from Proposition 5, yields a surrogate whose steady amplitudes, stability boundaries, folds and tongues converge to the exact ones as the sample size grows, at the approximation rate of Theorem 4.*

Proof. The coefficient map is smooth in the parameters, so Theorem 4 applies to $\mathcal{G}$. Uniform convergence of the coefficients implies convergence of the simple roots by Proposition 6, and the discriminant weighting ensures the fold set, where root convergence is only Holder continuous, is resolved; the tongue labels converge because they are certified by Proposition 5. □

6.1. From physical design variables to the operator inputs

The operator reads a five-component vector, and for the framework to sit inside a gradient-based design loop that vector has to be tied, with no gap left open, to the quantities an engineer fixes on a drawing. We record the tie here. Write the physical design vector as

$$\boldsymbol{d} = \big(\mathrm{br},\ T_0,\ \theta,\ L_0,\ EA_0,\ D_o,\ C_D,\ w_s,\ \gamma_v,\ \rho_w,\ \xi_s,\ \Omega_e\big), \tag{19}$$

collecting the buoyancy ratio, the pretension, the inclination, the chord, the axial stiffness, the outer diameter, the drag coefficient, the self-weight per unit length, the virtual mass per unit length, the water density, the structural damping ratio and the dimensional encounter frequency $\Omega_e = \omega_c \Omega$. The operator input is

$$p = \big(\delta,\ \hat{\nu},\ \hat{\xi}_s,\ \bar{K}_d,\ F^*\big) \text{ for LC1 and LC3}, \quad p = \big(\delta,\ \hat{\nu},\ \hat{\xi}_s,\ \bar{K}_d,\ \eta^* a_T\big) \text{ for LC2}. \tag{20}$$

The two are joined by a map $\mathcal{M} : \boldsymbol{d} \mapsto p$ that factors through three intermediate quantities. The first pair is the self-weight group and the elasto-geometric parameter of Definition 1,

$$\Gamma = \tfrac{w_s(1-\mathrm{br})L_0}{T_0}, \quad \varepsilon_0 = \tfrac{T_0}{EA_0}, \quad \lambda^2 = \tfrac{\Gamma^2 \cos^2\theta}{\varepsilon_0} = \tfrac{w_s^2(1-\mathrm{br})^2 L_0^2 \cos^2\theta \; EA_0}{T_0^3}. \tag{21}$$

The second and third are the characteristic scales already invoked in Section 3. The characteristic length is the sag of the equivalent horizontal tether and the characteristic frequency is that of the taut string,

$$L_c = \frac{\Gamma L_0}{8} = \frac{w_s(1-\mathrm{br})L_0^2}{8\,T_0}, \qquad \omega_c = \frac{\pi}{L_0}\sqrt{\frac{T_0}{\gamma_v}}. \tag{22}$$

Three components of p are then elementary explicit functions of $\boldsymbol{d}$, and they are written out below. The remaining two, the geometric coefficient $\hat{\nu}$ and the drive amplitude, are the algebraic outputs of the small-sag reduction of the study by Corazza et al. [1], which returns them as rational functions of λ^2, θ and η_0 together with the tube heave amplitude a_T delivered by Equation (4a); they are evaluated once per design and differentiated by the same algebra. **Table 1** records each input with the physical variables it carries. The two written out here are the ones carrying the design variables a conceptual study varies first. Substituting Equation (22) into Equation (5) puts the drag group in physical terms,

$$\bar{K}_d = \frac{16}{9\pi^2}\frac{C_D \rho_w D_o L_c}{\gamma_v} = \frac{2}{9\pi^2}\,\frac{C_D\,\rho_w D_o\, w_s(1-\mathrm{br})L_0^2}{\gamma_v\, T_0}, \tag{23}$$

and the resonance conditions of Section 3 put the detuning in physical terms,

$$\delta = \frac{1}{\varepsilon}\left(\frac{\Omega_e}{n\,\bar{\omega}\,\omega_c} - 1\right), \qquad n = 1 \text{ for LC1 and LC3}, \quad n = 2 \text{ for LC2}, \tag{24}$$

where $\bar{\omega} = \bar{\omega}(\lambda^2)$ solves the Irvine frequency relation of the first in-plane mode [3],

$$\tan\!\Big(\frac{\pi\bar{\omega}}{2}\Big) = \frac{\pi\bar{\omega}}{2} - \frac{4}{\lambda^2}\Big(\frac{\pi\bar{\omega}}{2}\Big)^3, \tag{25}$$

which returns $\bar{\omega} \to 1$ in the taut limit $\lambda^2 \to 0$ and so reproduces the reference value of **Table 2**.

Table 1. Map $\mathcal{M}$ from the physical design vector to the five operator inputs.

Operator input	Defining relation	Physical variables entering
δ, detuning	Equation (24) with Equation (25)	Ω_e, T_0, L_0, γ_v, br, θ, EA_0, w_s
$\hat{\nu}$, cubic coefficient	$\hat{\nu}_e = \hat{\nu} - \kappa\hat{\beta}^2/\bar{\omega}^2$ of Remark 1, with $\hat{\nu}$, $\hat{\beta}$ rational in λ^2 and θ	br, T_0, L_0, EA_0, θ, w_s through λ^2
$\hat{\xi}_s$, structural damping	$\hat{\xi}_s = \xi_s/\varepsilon$, a material property	ξ_s
$\hat{K}_d$, drag group	Equation (23) with $\hat{K}_d = \bar{K}_d/\varepsilon$	C_D, D_o, ρ_w, br, T_0, L_0, γ_v, w_s
F^*, forcing (LC1, LC3)	$(\bar{\alpha}\sin\theta + \zeta\cos\theta)a_T\bar{\omega}^2$	θ, λ^2, and a_T from Equation (4a)
$\eta^* a_T$, pump (LC2)	$2(\bar{\eta} - \bar{\mu})\sin\theta\, a_T$ of Equation (6)	θ, λ^2, η_0, and a_T from Equation (4a)

Table 2. Reference non-dimensional parameters used in the numerical experiments.

Symbol	Meaning	Value
$\bar{\omega}$	tether modal frequency	1.00
$\hat{\xi}_s$	structural damping coefficient	0.02
$\hat{K}_d$	drag-damping group	0.12
$\hat{\nu}$	effective cubic coefficient	1.00
F^*	LC1 and LC3 forcing amplitude	0.80
$\eta^* a_T$	LC2 parametric pump	1.00
ε	ordering parameter	0.02
δ	detuning (swept)	$[-20, 20]$

Each step is algebraic, save for $\bar{\omega}(\lambda^2)$, where Equation (25) is implicit and the implicit function theorem supplies the derivative. The map $\mathcal{M}$ is therefore differentiable and its Jacobian $\partial p/\partial \boldsymbol{d}$ is available in closed form. The entries produced by the two variables a conceptual study moves first are

$$\frac{\partial \bar{K}_d}{\partial \mathrm{br}} = -\frac{\bar{K}_d}{1-\mathrm{br}}, \quad \frac{\partial \bar{K}_d}{\partial T_0} = -\frac{\bar{K}_d}{T_0}, \quad \frac{\partial \lambda^2}{\partial \mathrm{br}} = -\frac{2\lambda^2}{1-\mathrm{br}}, \quad \frac{\partial \lambda^2}{\partial T_0} = -\frac{3\lambda^2}{T_0}, \tag{26}$$

alongside $\partial\delta/\partial T_0 = -(1+\varepsilon\delta)/(2\varepsilon T_0)$ at fixed $\bar{\omega}$, to which the implicit function theorem applied to Equation (25) adds the term transmitted through $\bar{\omega}(\lambda^2)$, a term that vanishes in the taut limit, $\partial\bar{K}_d/\partial C_D = \bar{K}_d/C_D$, $\partial\bar{K}_d/\partial L_0 = 2\bar{K}_d/L_0$, $\partial\lambda^2/\partial\theta = -2\lambda^2\tan\theta$ and $\partial(\eta^* a_T)/\partial\theta = \eta^* a_T \cot\theta$. Raising the buoyancy ratio or the pretension thus lightens the drag group and tautens the tether at rates that are known exactly rather than estimated by finite differences.

The design sensitivity of the response closes by the chain rule. At a simple root, implicit differentiation of $P(a; c(p)) = 0$ gives $\partial a/\partial p_j = -(\partial P/\partial p_j)/(\partial P/\partial a)$ in the sense of Proposition 6, so that

$$\frac{\partial a}{\partial d_i} = \sum_j \frac{\partial a}{\partial p_j}\frac{\partial p_j}{\partial d_i}, \tag{27}$$

the first factor coming from one backward pass through $\mathcal{G}$ and the second from Equation (26). A design loop therefore differentiates the amplitude with respect to buoyancy ratio, pretension, inclination and drag coefficient directly, and the same composition carries the distance to the nearest fold and the distance to the nearest tongue into the physical design space.

6.2. From the learned coefficients to the Floquet multipliers

The tongue chart of Proposition 5 is a statement about the linearization Equation (15), whereas the operator returns the coefficients of the response polynomial. The step joining the two is an exact algebraic inversion, and we write it out.

Proposition 8. *Let $c(p) = (c_4, c_3, c_2, c_1, c_0)$ be the coefficients of the LC2 response polynomial Equation (12) returned by $\mathcal{G}$ at a parameter value whose detuning coordinate is δ, let $\bar{\omega}$ be the known frequency normalization, and let the geometric* *nonlinearity and the drag group be present, so that* $c_4 > 0$ *and* $c_2 + 12\hat{\nu}\bar{\omega}^2\delta > 0$. *Then*

$$\begin{aligned} c_4 &= \tfrac{9}{4}\hat{\nu}^2, \quad c_3 = 0, \quad c_2 = 16\bar{\omega}^4\hat{K}_d^2 - 12\hat{\nu}\bar{\omega}^2\delta, \\ c_1 &= 32\bar{\omega}^4\hat{\xi}_s\hat{K}_d, \quad c_0 = 16\bar{\omega}^4(\hat{\xi}_s^2 + \delta^2) - (\eta^* a_T)^2. \end{aligned} \tag{28}$$

and the data of the linearization are recovered from c *in four steps,*

$$\begin{aligned} \hat{\nu} &= \tfrac{2}{3}\sqrt{c_4}, \qquad \hat{K}_d = \frac{\sqrt{c_2 + 12\hat{\nu}\bar{\omega}^2\delta}}{4\bar{\omega}^2}, \\ \hat{\xi}_s &= \frac{c_1}{32\bar{\omega}^4\hat{K}_d}, \qquad \eta^* a_T = \sqrt{16\bar{\omega}^4(\hat{\xi}_s^2 + \delta^2) - c_0}, \end{aligned} \tag{29}$$

and the pump depth of Equation (16) *is* $h = \varepsilon\,\eta^* a_T/\bar{\omega}^2$. *Substituting* h *and the damping ratio into Equation* (15) *and integrating the fundamental matrix over one pump period returns the Floquet multipliers of the zero solution, equivalently the recurrence Equation* (A6) *returns them through the Hill determinant. Moreover the first-order tongue boundary is the vanishing of the constant coefficient itself,*

$$c_0(p) = 0 \quad \Longleftrightarrow \quad h = h^* = 4\varepsilon\sqrt{\hat{\xi}_s^2 + \delta^2}, \tag{30}$$

the trivial state being linearly unstable exactly where $c_0(p) < 0$.

Proof. The identifications Equation (28) are read off Equation (12) monomial by monomial. The inversion Equation (29) then proceeds in the stated order: c_4 fixes $\hat{\nu}$ on the hardening branch $\hat{\nu} > 0$, c_2 fixes $\hat{K}_d > 0$ once $\hat{\nu}$ is known, c_1 fixes $\hat{\xi}_s$, and c_0 fixes the pump amplitude. Every step divides by a quantity that is nonzero whenever the geometric nonlinearity and the drag group are present, so the inversion is well defined and smooth in c. For the last claim, linearize the slow flow at vanishing amplitude. Dividing Equation (10) by a leaves the growth rate $-\hat{\xi}_s\bar{\omega} + (\eta^* a_T/4\bar{\omega})\sin\gamma$, and Equation (11) at a stationary phase leaves $\cos\gamma = -4\bar{\omega}^2\delta/(\eta^* a_T)$. Eliminating γ through $\sin^2\gamma + \cos^2\gamma = 1$, the growth rate is positive precisely when $(\eta^* a_T)^2 > 16\bar{\omega}^4(\hat{\xi}_s^2 + \delta^2)$, which by Equation (28) reads $c_0 < 0$; solving the equality for $\eta^* a_T$ and inserting it into Equation (16) gives the stated h^*. □

Three consequences follow. The tongue is decided by the single coefficient c_0, so it inherits the accuracy of the coefficient map directly and never passes through root extraction, which is the step whose conditioning degrades on the fold set. The boundary is a smooth function of the parameters, so the distance to the tongue can be differentiated and carried into a design constraint through Equation (27), exactly as the distance to a fold is. And the algebraic and the certified routes agree where they should. At zero detuning Equation (30) reduces to $h^* = 4\varepsilon\hat{\xi}_s$, four times the damping ratio of Equation (15) and the classical threshold of the principal tongue of the damped Mathieu equation; for the reference values this is 1.6000×10^{-3}, against 1.6000×10^{-3} from bisection on the monodromy matrix, an agreement to eight significant figures. At the reference pump depth $h = 0.02$ the algebraic boundary places the band edge at $\delta = 0.2492$ and the certified computation at $\delta = 0.2489$, and the response equation itself returns a nonzero amplitude from $\delta = -0.239$ onward, so the amplitude side, the algebraic side and the Floquet side of the same statement close on one another. Once the pump depth is of order unity the first-order boundary is no longer the exact one, and the recovered h is then passed to the Floquet computation of Proposition 5; the algebraic boundary is the leading term of that contour.

The computational cost of a query is dominated by a single forward pass of the operator, which is quadratic in the network width, followed by the extraction of the companion-matrix eigenvalues, which is cubic in the polynomial degree and therefore negligible since the degree is at most six, and by the evaluation of the resultant for the fold distance, which is a fixed small determinant. The parameter sensitivities are obtained by automatic differentiation through the same forward pass at the cost of one additional backward pass, which is what makes the surrogate directly usable inside a gradient-based design loop. In contrast, a direct integration query must resolve a long transient at each parameter value, and a high-fidelity query is more expensive still, so the operator is faster by several orders of magnitude, as quantified in Section 8.

The two pillars interlock. The network of Section 5 is the trusted engine that supplies labels where closed forms are inaccurate, and the operator of this section is the global, differentiable atlas that consumes them and returns, in real time, the amplitude, the stability, the distance to the nearest fold and the distance to the nearest tongue for any design. Together they cover the whole conceptual-design workflow: the network certifies accuracy at finite ordering parameter and in the order-unity parametric regime that the closed form cannot reach, and the operator turns that certified accuracy into a continuous and differentiable map across the design space.

7. Numerical experiments

Unless stated otherwise the non-dimensional parameters are those of **Table 2**, chosen to be representative of the Messina Strait tether studied in the study by Corazza et al. [1]. All response curves are computed from the exact roots of the frequency-response polynomials. All time-domain checks integrate the unreduced oscillator of Equation (4b) without the harmonic-balance simplification, and all Floquet quantities come from the numerically integrated monodromy matrix of Equation (15). The two networks are trained on different targets, as set out in Section 5 and Proposition 7. The slow-flow-informed network is trained on modulation transients obtained by integrating Equation (10) and Equation (11) for LC2, or Equation (13) for LC1 and LC3, and the operator is trained on parameter samples whose targets are the real positive roots of the response polynomials. Neither is trained on any time series of Equation (4b), which is held back for testing.

The values in **Table 2** are the order-unity coefficients, that is the hatted quantities of Equation (7) as they enter the slow flow and the response polynomials. The corresponding physical ratios in the tether equation Equation (4b) carry a factor ε: the structural damping ratio is $\xi_s = \varepsilon\hat{\xi}_s = 4 \times 10^{-4}$, the drag group of Equation (5) is $\bar{K}_d = \varepsilon\hat{K}_d$, and the pump depth of Equation (16) at the reference pump is $h = \varepsilon\,\eta^* a_T/\bar{\omega}^2 = 0.02$.

The narrow-band character of the wave input, which justifies the harmonic idealization of the loading, is shown in **Figure 3** for two significant wave heights. The validation of the response equations against the unreduced oscillator is reported in **Figure 4**. The forced conditions LC1 and LC3 share the sextic Equation (14) up to the replacement of F^* by the direct forcing $\tilde{f}$, so one curve carries both and they are drawn together in the left panel, while the parametric condition LC2, governed by the quartic Equation (12), occupies the right panel. Each marker is obtained by starting the unreduced oscillator on the predicted branch, with the phase fixed by the relations Equation (A4) or Equation (A5), and integrating over a slow interval of two hundred units; the settled half range of the response is the plotted amplitude. The markers sit on the curve through the resonance and along both flanks, including the upper branch within the fold interval. The LC2 response is nonzero only in a narrow band of detuning, which is the parametric tongue seen from the amplitude side.

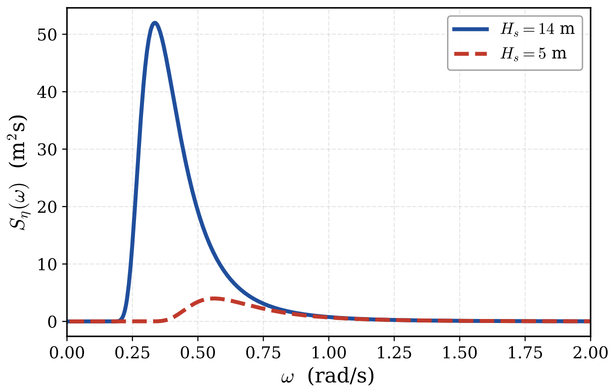

Figure 3. Narrow-band wave elevation spectra for two significant wave heights, justifying the harmonic idealization of the hydrodynamic input adopted in the analysis. The horizontal axis is the wave angular frequency ω in rad/s and the vertical axis is the elevation spectral density $S_\eta(\omega)$ in m^2 s; the two curves correspond to significant wave heights $H_s = 14\,\mathrm{m}$ and $H_s = 5\,\mathrm{m}$.

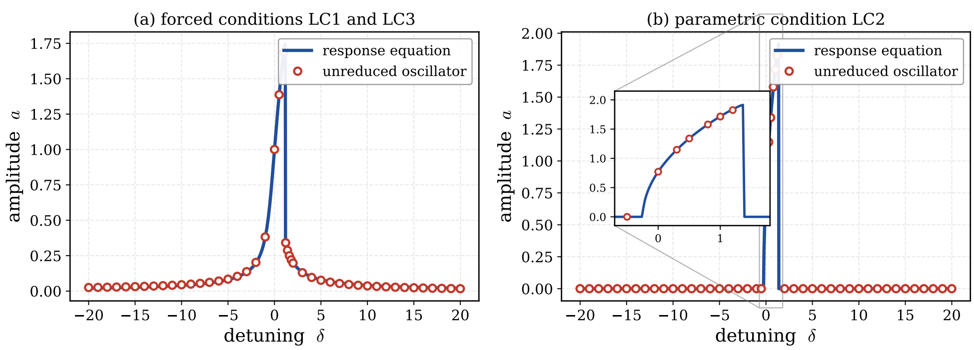

Figure 4. Validation of the response equations against direct integration of the unreduced oscillator Equation (4b), with parameters from **Table 2**. **(a)** the forced conditions LC1 and LC3, which share the sextic Equation (14) up to the substitution $F^* \mapsto \tilde{f}$. **(b)** the parametric condition LC2, governed by the quartic Equation (12), whose response is confined to a narrow band of detuning. In both panels the solid curve is the amplitude a against the detuning δ and the open markers are the settled amplitudes of the unreduced oscillator.

A quantitative summary of the agreement is given in **Table 3**, which reports the root-mean-square deviation between the response equation and direct integration of the unreduced oscillator over the swept detuning range and over the near-resonant band, together with the largest single deviation. Both conditions agree to better than a quarter of a per cent of the peak amplitude. The largest single deviations arise where the branch approaches a fold, and there the two coalescing steady states lie closer together than the deviation quoted, so what is being measured is the sensitivity of the steady state itself rather than an error of the reduction.

Table 3. Deviation between the response equation and direct integration of the unreduced oscillator.

Condition	RMSE (all δ)[a]	RMSE (near)[b]	Max deviation[c]	Peak amplitude
LC1 and LC3 (forced)	0.0041	0.0039	0.0057	1.744
LC2 (parametric)	0.0021	0.0035	0.0138	1.915

Note: [a] Root-mean-square deviation between the amplitude of the response equation and direct integration of Equation (4b) over the swept range $\delta \in [-20, 20]$. LC1 and LC3 share one row because they share the response equation Equation (14) up to the substitution $F^* \mapsto \tilde{f}$. Each time-domain run starts on the predicted branch with the phase set by Equation (A4) or Equation (A5) and is advanced over a slow interval of two hundred units. [b] Restricted to the near-resonant band $|\delta| \leq 5$. [c] The largest single deviations occur where the branch approaches a fold. There the coalescing steady states are separated by less than the deviation quoted, so the figure measures the sensitivity of the steady state and not an error of the reduction.

A phenomenon specific to submerged tethers is the closure of the response branch by the amplitude-dependent damping, shown in **Figure 5**. The dry cable, for which the drag group vanishes, retains an open hardening branch, while the submerged cable has a closed branch of bounded amplitude, exactly as predicted by the odd monomial of Equation (14). The influence of the drag group is quantified in **Figure 6**, again with the forced pair on the left and the parametric condition on the right, since a separate sweep for LC3 would repeat the LC1 curves point for point. Raising the drag group lowers and rounds the peak, and the effect is the stronger of the two for the parametric condition. The role of the geometric nonlinearity is shown in **Figure 7**, where increasing the cubic coefficient bends the response and widens the hysteretic interval, and the role of the forcing amplitude is shown in **Figure 8**, where the peak grows and the fold interval widens with the drive. The locus of peak amplitude as the forcing varies traces the backbone curve of **Figure 9**.

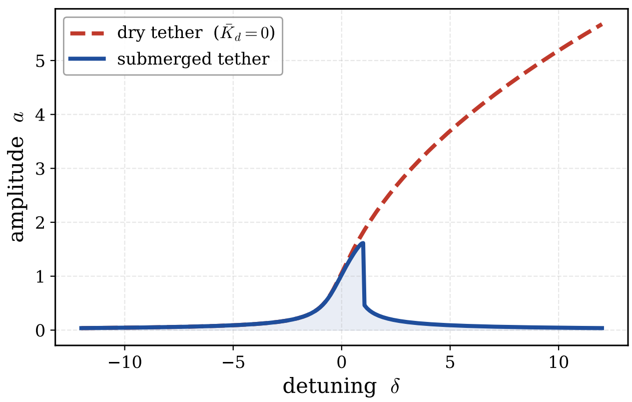

Figure 5. Branch closure: the amplitude-dependent fluid damping closes the submerged branch that stays open for a dry cable. Amplitude a against detuning δ; the dashed curve is the dry cable ($\bar{K}_d = 0$) and the solid curve the submerged tether ($\bar{K}_d > 0$), whose drag term bounds the amplitude and turns the branch back.

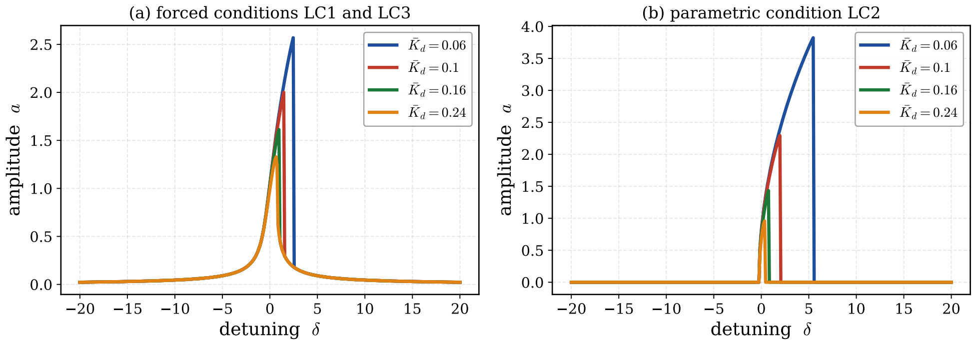

Figure 6. Response for several drag groups, $\bar{K}_d \in \{0.06, 0.10, 0.16, 0.24\}$, with amplitude a against detuning δ. **(a)** The forced conditions LC1 and LC3. **(b)** The parametric condition LC2, where the drag group has the stronger effect. A larger drag group lowers and rounds the resonant peak in both.

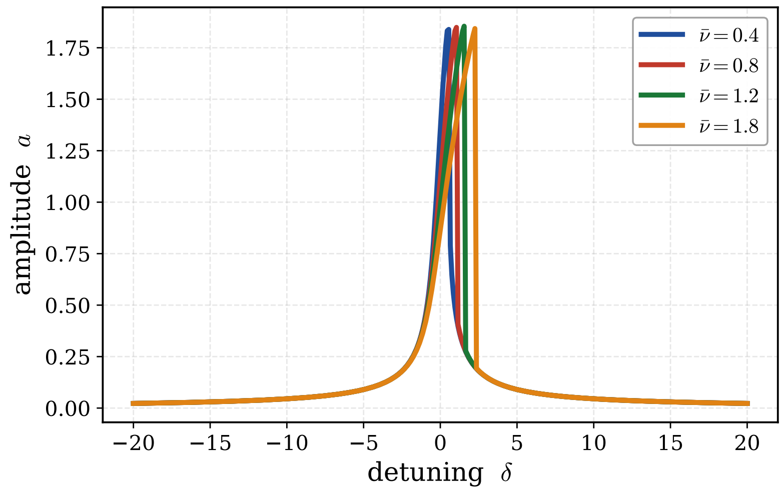

Figure 7. Effect of the cubic geometric coefficient on the LC1 response. Amplitude a against detuning δ for $\bar{\nu} \in \{0.4, 0.8, 1.2, 1.8\}$; a larger cubic coefficient bends the response and widens the hysteretic interval.

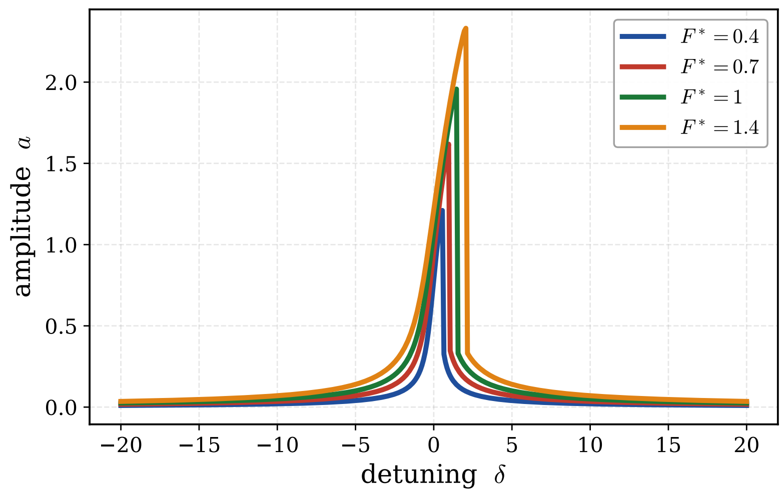

Figure 8. Effect of the forcing amplitude on the LC1 response. Amplitude a against detuning δ for $F^* \in \{0.4, 0.7, 1.0, 1.4\}$; the peak and the fold interval grow with the drive.

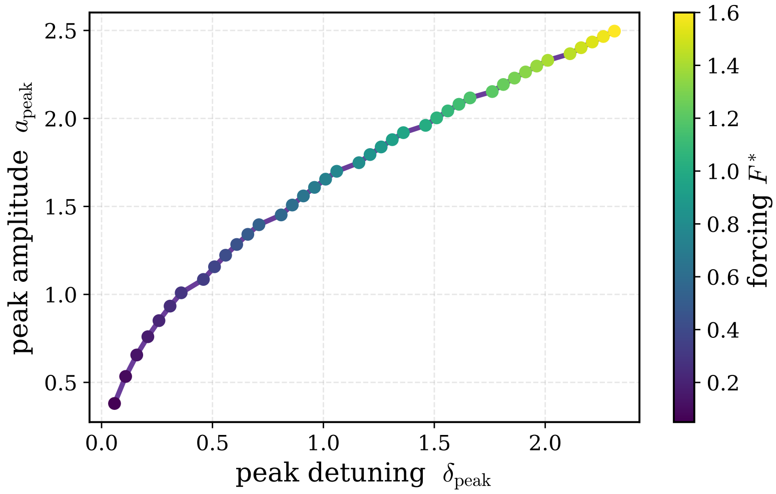

Figure 9. Backbone curve traced by the peak as the forcing varies. Locus of the response peak in the peak-detuning versus peak-amplitude plane; the color bar is the forcing amplitude F^*.

The response manifold over the detuning and forcing plane is shown in **Figure 10**, and the slow-flow phase portraits that underlie it are shown in **Figure 11**, with the forced condition LC1 on the left and the Mathieu-Duffing condition LC2 on the right, where the steady amplitudes appear as the radii of the limit sets and the trajectories spiral onto the stable fixed point. The bifurcation set is mapped in **Figure 12**, which shows the number of coexisting states over the detuning and drag-group plane and the fold curves that separate the cells of Proposition 3, and in **Figure 13**, which exhibits the cusp of Proposition 4 where two fold curves meet in the detuning and forcing plane. The parametric-instability tongue of Proposition 5 is shown in **Figure 14** as the region where the largest Floquet multiplier exceeds unity, and the coexistence count over the detuning and forcing plane is shown in **Figure 15**.

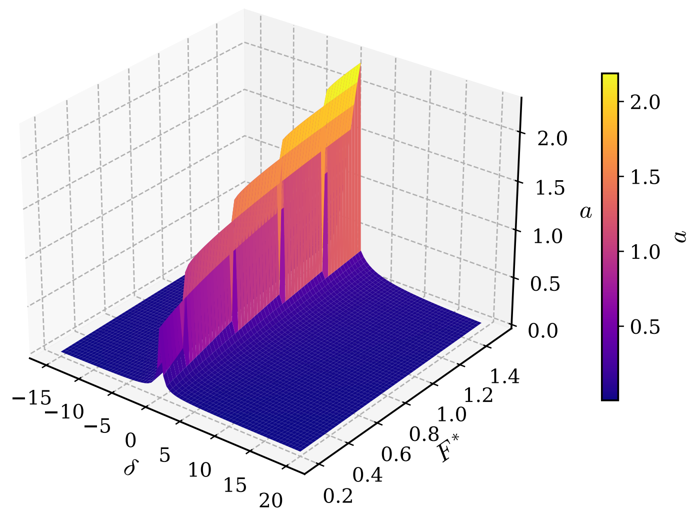

Figure 10. Steady-state response manifold over the detuning and forcing plane for LC1, showing the folded hardening peak whose overhang encloses the region of coexisting states. The horizontal axes are the detuning δ and the forcing amplitude F^*, and the surface height and color are the steady amplitude a.

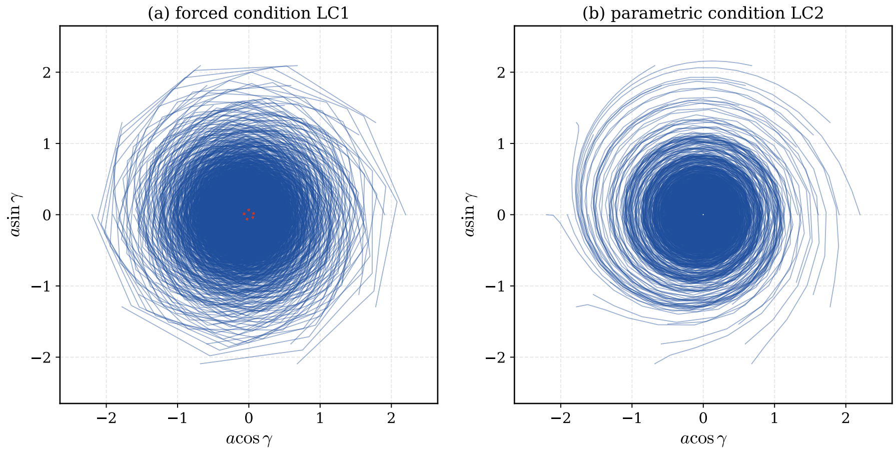

Figure 11. Slow-flow phase portraits in the Cartesian slow plane $(a\cos\gamma, a\sin\gamma)$, with trajectories spiraling onto the stable fixed point and the dotted rings marking the steady amplitudes. **(a)** The forced condition LC1. **(b)** The Mathieu-Duffing condition LC2.

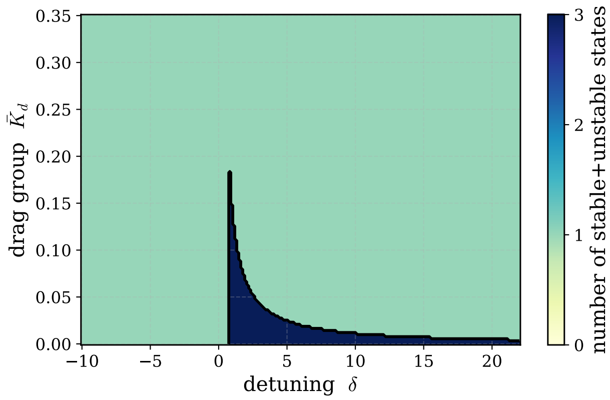

Figure 12. Bifurcation set over the detuning and drag-group plane, with fold curves separating regions of different state count. Axes are the detuning δ and the drag group $\bar{K}_d$; the color bar counts the coexisting steady states (0 to 3) and the black curves are the saddle-node fold loci of Proposition 3.

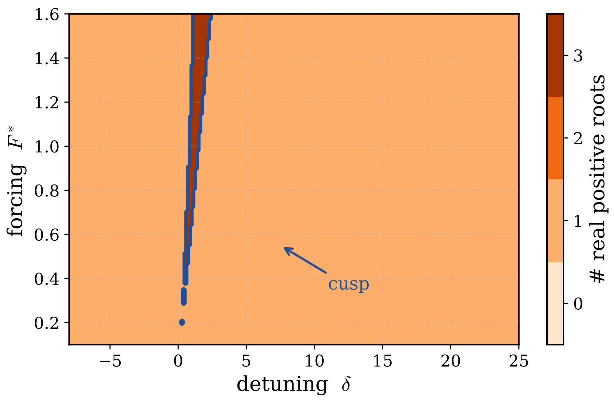

Figure 13. Cusp organizing center where two fold curves meet. Axes are the detuning δ and the forcing amplitude F^*; the color encodes the number of real positive roots and the marked point is the cusp of Proposition 4, where the two saddle-node fold curves meet tangentially and the bistable region is born.

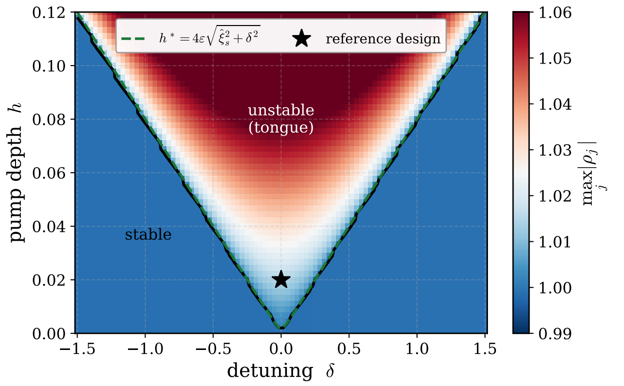

Figure 14. Parametric-instability tongue from the Floquet analysis. Axes are the detuning δ and the pump depth h, the latter being the stiffness modulation of Equation (16), $h = \varepsilon\,\eta^* a_T/\bar{\omega}^2$, with the damping ratio set to $\varepsilon\hat{\xi}_s = 4\times10^{-4}$. The color bar is the largest Floquet multiplier $\max_j|\rho_j|$ and the black contour $\max_j|\rho_j| = 1$ is the stability boundary of Proposition 5. Inside the tongue the rest state is unstable and a finite vibration grows from rest. The dashed curve is the algebraic boundary $h^* = 4\varepsilon\sqrt{\hat{\xi}_s^2+\delta^2}$ of Proposition 8 and the star marks the reference design of **Table 2**.

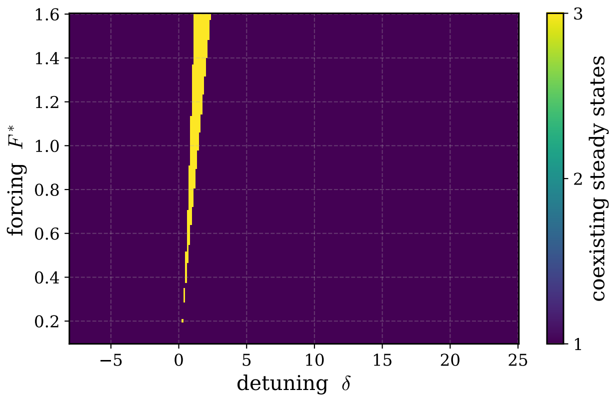

Figure 15. Number of coexisting steady states over the detuning and forcing plane. Axes are the detuning δ and the forcing amplitude F^*; the color bar counts the coexisting steady states.

These bifurcation diagnostics are the practical payload of the analysis. The fold curves of **Figure 12** delimit the region of the design space in which two stable states coexist, a situation that a fatigue assessment must flag because the structure can jump between branches under a perturbation, and the cusp of **Figure 13** is the codimension-two point at which that coexistence region is born, so it marks the most sensitive location of the design space. The parametric tongue of **Figure 14** identifies the combinations of detuning and pump depth for which the rest state is unstable and a finite vibration is triggered even in the absence of direct forcing, which is the mechanism most easily overlooked by a purely forced analysis. The fact that all three diagnostics are recovered from one polynomial representation, by algebra and by a certified Floquet computation rather than by repeated simulation, is what makes the framework usable at the conceptual stage.

The uniform-in-time property of Theorem 5 is demonstrated in **Figure 16**, which compares the unreduced oscillator, the slow-flow reconstruction and a naive perturbation over time, and in **Figure 17**, which shows that the running maximum error of the slow-flow reconstruction stays bounded while that of the naive perturbation saturates at order one. A network trained to represent the slow amplitude reproduces the modulation transient in **Figure 18**.

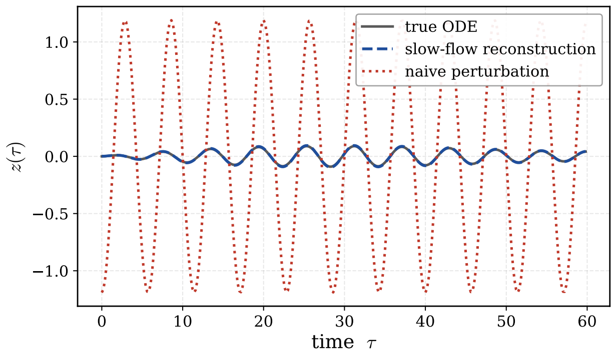

Figure 16. True oscillator, slow-flow reconstruction and naive perturbation over time. Displacement $z(\tau)$ against time τ at ordering parameter $\varepsilon = 0.05$; the slow-flow reconstruction tracks the true response while the naive regular perturbation drifts out of phase.

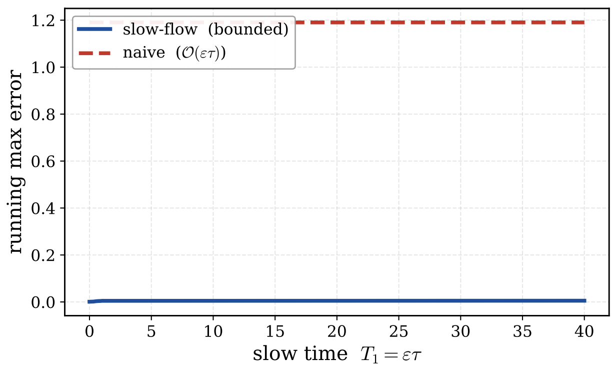

Figure 17. Running maximum error: bounded for the slow flow, saturating for the naive expansion. Running maximum of $|z - \hat{z}|$ against slow time $T_1 = \varepsilon\tau$; the naive curve saturates at order one, the slow-flow curve stays bounded.

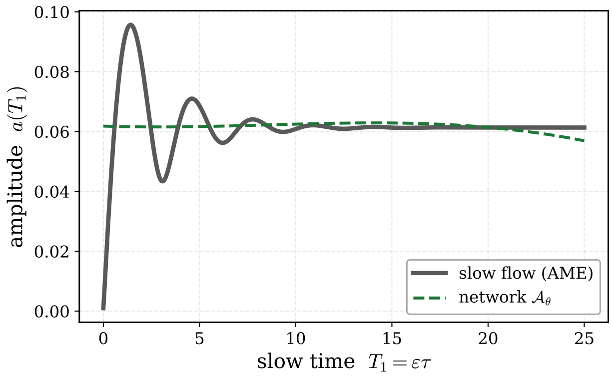

Figure 18. Network representation of the slow amplitude against the modulation solution. Slow amplitude $a(T_1)$ against slow time $T_1 = \varepsilon\tau$; the network output overlays the solution of the modulation equations.

How the two pillars behave as the ordering parameter is raised is examined in **Figure 19**. The sweep starts at $\varepsilon = 0.02$, passes through the values a conceptual study meets in practice, 0.05 and 0.10, and continues to 0.30, well outside the range in which the asymptotic reduction was constructed.

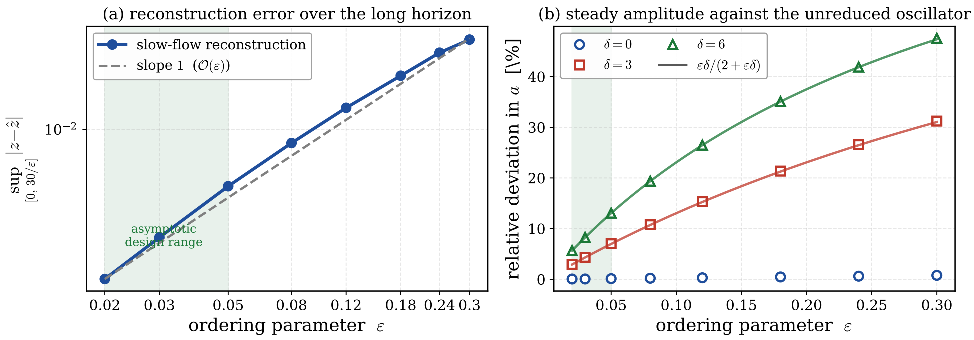

Figure 19. Behavior over an extended range of the ordering parameter, $\varepsilon \in [0.02, 0.30]$, with the band $\varepsilon \leq 0.05$ shaded. **(a)** Maximum reconstruction error over the horizon on logarithmic axes, against the unit-slope line of the $\mathcal{O}(\varepsilon)$ bound of Equation (18). **(b)** Relative deviation of the steady amplitude from the unreduced oscillator at three detunings, against the law $\varepsilon\delta/(2+\varepsilon\delta)$ that the linearization of the frequency offset predicts.

The left panel confirms the order-ε scaling of Equation (18), and confirms it over the whole sweep rather than over its lower end alone. The maximum reconstruction error grows from 1.9×10^{-3} at $\varepsilon = 0.02$ to 2.8×10^{-2} at $\varepsilon = 0.30$, and the points sit on a unit-slope line with the same constant at both ends. The slow-flow representation therefore extrapolates without penalty, and it does so for a structural reason rather than by luck: the network carries the modulation field alone, that field stays smooth and low-dimensional as ε grows, and so the target the network must represent never becomes harder. What grows is the $\mathcal{O}(\varepsilon)$ truncation term of Equation (18), and it grows at exactly the rate the theorem predicts.

The right panel examines the steady amplitude, which is the quantity the operator returns. The departure here is governed by the product $\varepsilon\delta$ rather than by ε alone, that is by the fractional offset of the excitation frequency from resonance, which is the quantity the reduction assumes small. At the resonance the deviation from the unreduced oscillator stays below 0.8% all the way to $\varepsilon = 0.30$. Off resonance it follows $\varepsilon\delta/(2 + \varepsilon\delta)$, the difference between the linearized frequency offset $2\bar{\omega}^2\varepsilon\delta$ carried by the reduction and the exact offset $\bar{\omega}^2\varepsilon\delta(2 + \varepsilon\delta)$; at $\delta = 6$ this amounts to 13.0% at $\varepsilon = 0.05$ and 47.5% at $\varepsilon = 0.30$, and the measured points fall on that law to within two tenths of a percentage point.

Two readings follow for practice. Inside the band $\varepsilon \lesssim 0.05$ shaded in **Figure 19**, both pillars hold to a few per cent across the swept detuning, and that band covers the ordering parameters a submerged-tether design presents. Outside it the operator stays reliable near the resonant peak and near the tongue edges, which are the design-critical regions, while its accuracy on the far flanks degrades in the way just quantified. The degradation is also correctable without new theory, since the deviation is a known function of $\varepsilon\delta$: retaining the exact frequency offset in place of its linearization removes the leading part of it, and the slow-flow network, being trained on the modulation equations rather than at a fixed ε, supplies corrected labels at any ordering parameter for which the modulation description itself still carries meaning.

The operator of Section 6 is trained on parameter samples with the closed-form maximum amplitude as target. This experiment exercises the amplitude output of the operator, which is the quantity for which the response equation supplies a scalar label. The coefficient output is the one carrying the bifurcation content, and it enters the fold, cusp and tongue diagnostics through the exact algebra of Proposition 3, Proposition 4 and Proposition 8 rather than through a fitted amplitude. Its training loss and test accuracy are shown in **Figure 20**, with a test coefficient of determination of 0.969, and the parity of predicted against true amplitude is shown in **Figure 21**. The learned response surface is compared with the exact one in **Figure 22**, and the analytic sensitivity of the amplitude to the detuning, obtained by differentiating the surrogate, is compared with the exact sensitivity in **Figure 23**. The hyperparameters of the two networks are listed in **Table 4**, and the quantitative accuracy of the surrogate is summarized in **Table 5**.

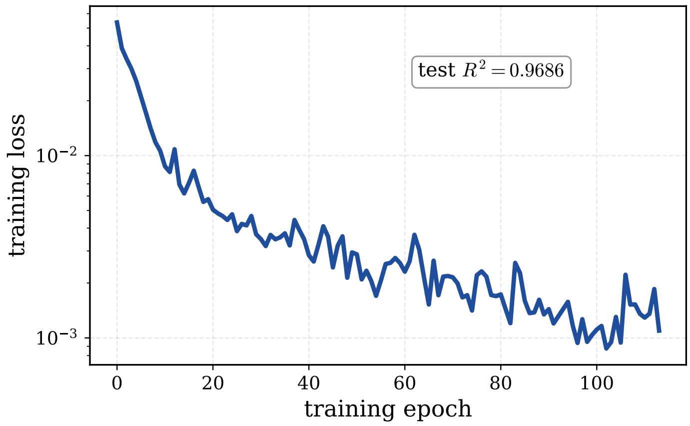

Figure 20. Operator training loss and test accuracy. Training loss against epoch on a logarithmic vertical axis; the held-out test coefficient of determination is $R^2 = 0.969$, with further metrics in **Table 5**.

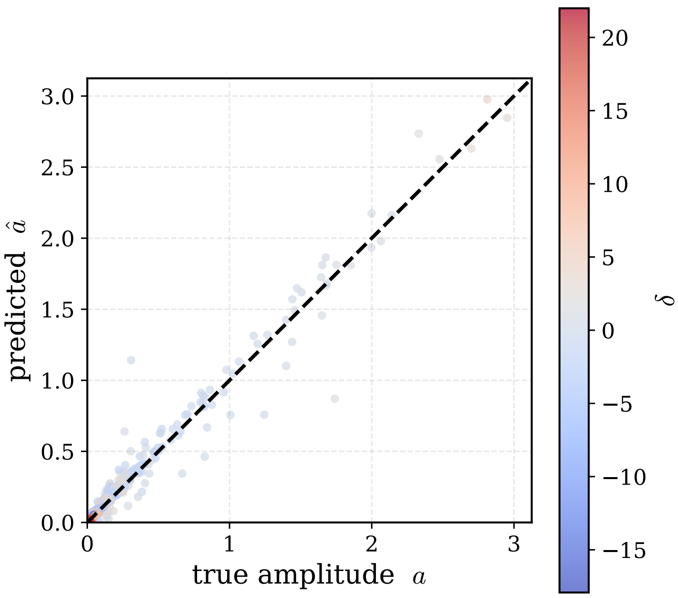

Figure 21. Parity of predicted against true amplitude on the test set. Predicted amplitude $\hat{a}$ against true amplitude a; points on the diagonal are exact and the color encodes the detuning δ.

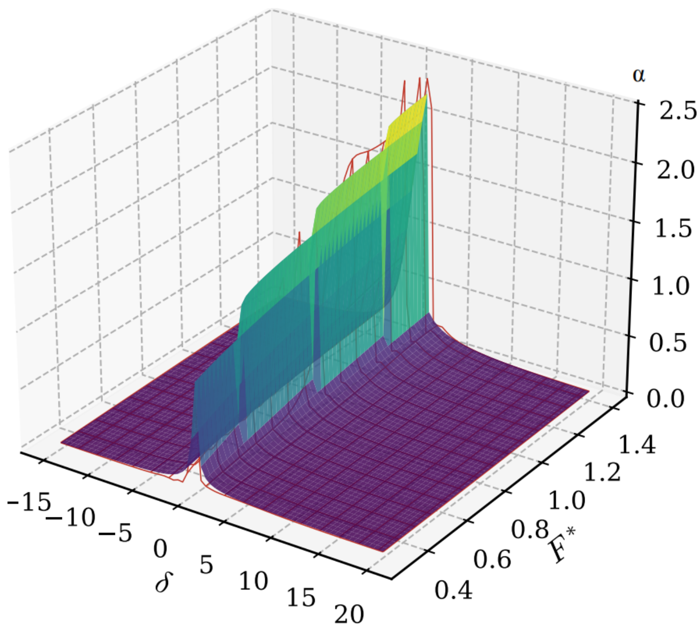

Figure 22. Learned response surface (wireframe) against the exact surface (shaded) over the detuning and forcing plane, showing that the operator reproduces the folded overhang and not merely the smooth flanks. The horizontal axes are the detuning δ and the forcing amplitude F^* and the height is the amplitude a; the shaded surface is exact and the wireframe is learned.

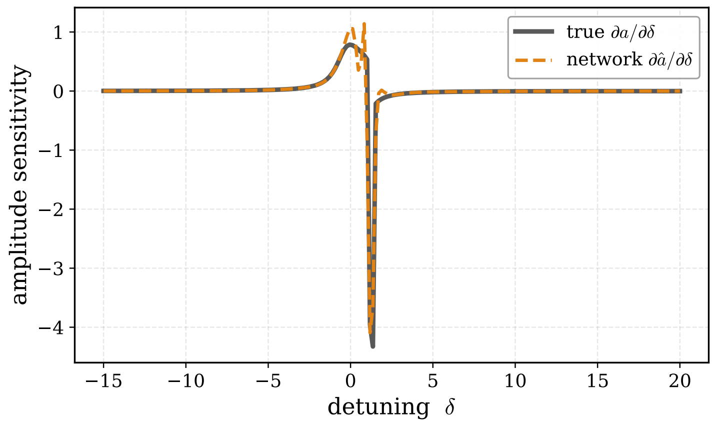

Figure 23. Analytic amplitude sensitivity to the detuning obtained by differentiating the surrogate, against the exact sensitivity, confirming that the learned map is differentiable and quantitatively usable inside a design loop. The sensitivity $\partial a/\partial\delta$ is plotted against the detuning δ; the surrogate curve is obtained by differentiating the learned map and the reference curve from the exact response.

Table 4. Network hyperparameters for the two learning pillars.

Setting	Slow-flow-informed network	Bifurcation-aware operator
hidden layers	2×40	3×96
activation	hyperbolic tangent	hyperbolic tangent
inputs	slow time	five design parameters
outputs	amplitude and phase	response amplitude
optimizer	quasi-Newton and Adam	Adam
training samples	modulation transient	$4,500$

The agreement of the sensitivity in **Figure 23**, and not only of the amplitude, is the property that matters for optimization, because a surrogate that fits the response but not its gradient would mislead any gradient-based search. The surrogate reproduces the sign changes of the sensitivity at the flanks of the resonance and the steep variation across the peak, which are exactly the features a design update must respect.

Table 5. Quantitative accuracy of the bifurcation-aware operator on the held-out test set.

Metric	Value
Coefficient of determination R^2	0.969
Root-mean-square error	0.053
Mean absolute error	0.016
Maximum absolute error [a]	0.87
Training/test samples	$4,500/1,200$

Note: [a] The largest errors localize on the fold set, where the maximal-amplitude target is discontinuous; away from the folds the error is at the level of the root-mean-square value.

Finally, the convergence of the certified tongue boundary with the Hill truncation order of Proposition 5 is shown in **Figure 24**, where the onset pump depth stabilizes rapidly, confirming the geometric convergence asserted in the proof.

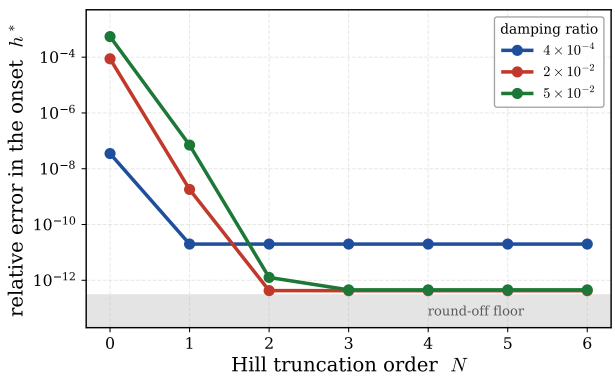

Figure 24. Convergence of the tongue onset with the Hill truncation order at zero detuning, for three damping ratios. Plotted is the relative deviation of the onset h^* returned by the truncated determinant of **Appendix B** from the value returned by bisection on the monodromy matrix. The leading truncation $N = 0$ already gives h^* equal to four times the damping ratio, and each further order contracts the deviation by roughly two decades until the round-off floor of the determinant is reached, which is the geometric rate asserted in Proposition 5. The certified onsets are 1.60000×10^{-3}, 8.00070×10^{-2} and 2.001093×10^{-1} for damping ratios 4×10^{-4}, 2×10^{-2} and 5×10^{-2} respectively.

8. Comparison with existing approaches

8.1. Accuracy and cost against numerical and analytical baselines

It is useful to place the framework against the established alternatives for predicting tether response, both in accuracy and in cost. The high-fidelity route is computational fluid dynamics coupled to finite-element structural models, as used in the coupled analyses of Jin and Kim [8] and in the nonlinear random-vibration study of Wang, Er and Iu [9]. It is the most faithful and also the most expensive, which leaves it unsuited to the wide sweeps of conceptual design. Direct numerical integration of the reduced model, as performed for validation [1], is far cheaper. It still requires a long transient at each parameter value, and it does not expose the bifurcation structure.

The closed-form multiple-scales solution [1] is essentially free once derived, but it is limited to first order in the ordering parameter, it breaks down for the order-unity pump, and it yields only static slices. The two pillars proposed here retain the accuracy of the closed form where it is valid, extend it with controlled error where it is not, and add the differentiable, bifurcation-resolved design manifold that none of the alternatives provide. The relative query costs are compared in **Figure 25**, and the qualitative capabilities are summarized in **Table 6**.

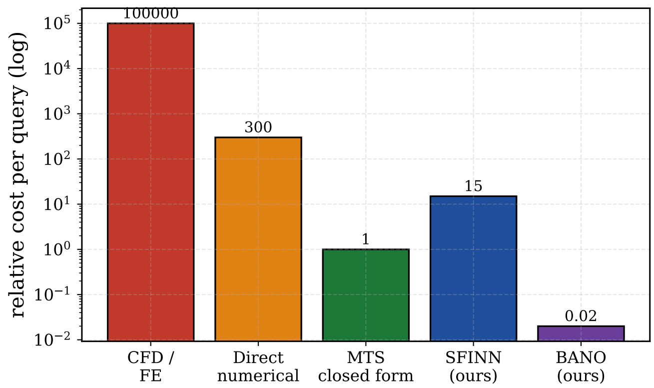

Figure 25. Relative cost per response query across methods, on a logarithmic scale. The cost is normalized so that one closed-form multiple-scales evaluation is unity; the bars are, from left to right, coupled CFD and finite element, direct numerical integration, closed-form multiple scales, the slow-flow-informed network and the bifurcation-aware operator. The operator query is several orders of magnitude cheaper than direct integration.

Table 6. Qualitative comparison of methods for conceptual tether-response prediction.

Method	Accuracy	Cost	Bifurcations	Sensitivities
CFD and finite element [8]	very high	very high	implicit	no
Direct integration [1]	high	moderate	implicit	no
Closed-form multiple scales [1]	first order	negligible	partial	no
Slow-flow network (this work)	controlled	low	yes	yes
Bifurcation operator (this work)	controlled	very low	yes	yes

The comparison confirms that the framework occupies a favorable point in the accuracy-cost plane, matching the closed form in its regime of validity, extending it with certified error control beyond that regime, and providing the bifurcation structure and the analytic sensitivities that conceptual design and fatigue screening require.

8.2. Relation to physics-informed and operator-learning architectures

It is worth setting the two pillars against the two learning architectures they are most naturally compared with, the physics-informed neural network and the deep operator network. A physics-informed network in the sense of Definition 10 places the residual of the governing equation at collocation points and minimizes it directly. Applied to Equation (4b), such a network has to resolve the fast carrier oscillation over the whole horizon, and it is on exactly this kind of stiff, multiscale and long-time problem that collocation training is known to stall, through the spectral bias and optimization pathologies reported by Krishnapriyan and co-workers [36] and by Wang and co-workers [37]; the reconstruction then accumulates the secular $\mathcal{O}(\varepsilon\tau)$ error of a regular expansion. The slow-flow-informed network removes this through an asymptotic preprocessing step: it represents only the slow amplitude and phase, the fast oscillation is carried analytically, and the error stays uniform over the long horizon by Theorem 5, so the secular growth never appears. A deep operator network of the DeepONet or Fourier-neural-operator type [38, 39] would instead regress the response amplitude on the parameters. Because that amplitude is multivalued across the folds, the regression is ill-posed precisely where the design-critical behavior lives, and it returns neither the stability of a branch nor the location of a fold or a tongue. The bifurcation-aware operator sidesteps this by learning the coefficients of the response polynomial rather than the amplitude, after which amplitudes, stability, folds, cusps and tongues follow by exact algebra and a certified Floquet computation. In short, the asymptotic preprocessing eliminates the secular long-time error that a plain physics-informed network inherits, and the structure-preserving output eliminates the multivaluedness that a plain operator-regression network cannot represent. Recent marine surrogates, such as the neural-operator reconstruction of Wan and co-workers [45] and the physics-informed cable model of Dan and co-workers [46], share the general tools but not these two safeguards.

9. Conclusion

We have developed an asymptotic-informed and bifurcation-aware learning framework for the nonlinear vibration of the anchoring tethers of a submerged floating tunnel, built on the reduced-order model of the coupled tube-tether system. On the analytical side we derived in detail the slow flow of the tether equation for the indirectly forced, the indirectly parametric and the directly forced loading conditions, we proved that the fixed points of the slow flow coincide to first order with the real positive roots of the closed-form frequency-response equations, and we characterized the local stability, the saddle-node folds through the amplitude resultant, the cusp organizing centers through elimination theory, and the parametric-instability tongues through a certified Floquet analysis. On the learning side we constructed a slow-flow-informed network whose reconstruction error we proved to be uniform over the long horizon on which naive collocation fails, and a bifurcation-aware operator that learns the response in polynomial form so that amplitudes, stability, folds, cusps and tongues are recovered by exact algebra and certified computation. The numerical experiments validate the closed forms against direct integration of the unreduced oscillator, reproduce the branch-closure effect that distinguishes a submerged from a dry tether, chart the parametric tongues in the order-unity regime that classical charts cannot reach, and deliver a differentiable design manifold with analytic sensitivities at a query cost several orders of magnitude below direct simulation, with a test coefficient of determination of 0.969. The framework therefore provides a fast, accurate and bifurcation-resolved instrument for the conceptual design and the fatigue screening of seabed-anchored submerged floating tunnels.

The framework is built to meet measurement rather than to stand apart from it, and the route from the present model to an instrumented crossing falls into four stages.

The first stage is instrumentation. What the framework needs is the tether amplitude and the tube heave, both resolved in frequency, together with the tether tension. An inclinometer array placed along a submerged line reconstructs displacement, angle and curvature in real time once the placement has been optimized, as Jin and Hong [51] show for this class of line, and non-contact stereo-vision measurement of mooring tension, developed by Lian and co-workers [52] for offshore floating platforms, supplies the tension channel without disturbing the line.

The second stage is identification of the two damping parameters, which is where the model is most sensitive and where measurement is most informative. The structural ratio $\hat{\xi}_s$ and the drag group $\bar{K}_d$ separate cleanly in a decay record, because Equation (5) makes the equivalent damping affine in the amplitude. Fitting the logarithmic decrement of a free-decay envelope against the instantaneous amplitude returns $\hat{\xi}_s$ as the intercept and $\bar{K}_d$ as the slope, and neither the drag coefficient nor the added mass has to be known on its own. Repeating the fit on forced records at several sea states supplies the redundancy that turns it into an estimate carrying a confidence interval.

The third stage is updating. With $\hat{\xi}_s$ and $\bar{K}_d$ measured and the remaining inputs computed from the drawing through **Table 1**, the operator is evaluated at the identified design point and, where the residual against the measured amplitudes warrants it, fine-tuned on the measured pairs. The physics-informed identification of a moored buoy by Li, Lu and Cao [50] shows that motion estimation and parameter identification can be carried inside one network, and the same construction transfers here with the modulation equations in place of the rigid-body equations.

The fourth stage tests the prediction that a purely forced analysis cannot make. Measured tube-heave spectra fix the pump depth through Equation (16), the operator returns the tongue through Proposition 8, and the question is whether tether vibration is observed to grow from rest inside the predicted band of encounter frequency. A crossing that never enters the band still furnishes a bound on the pump depth from above, so a null result carries information too.

Past calibration, the most substantial modeling extension is damping with memory. The quadratic drag of Definition 3 acts instantaneously, whereas the sheathing of a real tether is viscoelastic and the surrounding fluid retains a wake, so the force at an instant depends on the history of the motion. A fractional-derivative constitutive term is the standard vehicle for that dependence, and it has already been carried through the asymptotic machinery used here: Luo and co-workers [53] treat a fractional oscillator by multiple scales, Tang, Wang and Ding [54] settle the parametric stability of fractionally viscoelastic pipes conveying fluid, and Lian and co-workers [55] analyze free nonlinear vibration under a fractional damping kernel. Such a term makes the slow flow itself fractional in the slow time, so the modulation equations acquire a memory kernel and their fixed points cease to follow from a polynomial alone. Both pillars accommodate that change, and the learning machinery for the non-local operators it produces is reviewed by Tian, Peng and He [56], who set out how a fractional derivative is discretized inside a training loss and how the fractional order itself is identified from data. The second capability matters here, since the order of the damping kernel is exactly what a field record would have to supply.

Three directions remain open on the theoretical side. The response manifold can be carried to a generalized metric coupling the heave and sway motions. The slow-flow representation can absorb broadband stochastic wave excitation in place of the harmonic idealization. And the operator can be taken to time-delay tether systems in which feedback or control introduces a lag. On the engineering side the framework invites the analysis of multi-tunnel arrays whose neighboring tethers interact hydrodynamically.

Author contributions: Conceptualization, MA and UI; methodology, MA, UI and ILP; formal analysis, MA and ILP; software and numerical experiments, UI; validation, MA, UI and ILP; writing of the original draft, UI; review and editing, MA and ILP; visualization, UI; supervision, MA. All authors have read and agreed to the published version of the manuscript.

Funding: This research work was funded by the Deanship of Scientific Research, Islamic University of Madinah, Saudi Arabia.

Institutional review board statement: Not applicable.

Informed consent statement: Not applicable.

Data availability statement: The data supporting the reported results, together with the scripts that reproduce the figures, are available from the corresponding author upon reasonable request.

Acknowledgment: The authors extend their appreciation to the Deanship of Scientific Research, Islamic University of Madinah, Saudi Arabia, for funding this research work.

Conflict of interest: The authors declare no conflicts of interest.

AI use statement: The authors declare that no artificial intelligence (AI) tools were used in the preparation of this manuscript

Abbreviation

z	tether modal coordinate	$\bar{w}_T$	tube heave, w_T/L_c
τ	non-dimensional time	ε	ordering parameter
$\bar{\omega}$	tether modal frequency	$\bar{\omega}_{T,v}$	tube modal frequency
ξ_s	structural damping ratio	ξ_{eq}	drag-induced equivalent damping
$\hat{\xi}_s, \hat{K}_d, \hat{\nu}$	order-unity coefficients	Ω_e	dimensional encounter frequency
$\bar{K}_d$	drag-damping group	$\bar{\beta}$	quadratic geometric coefficient
$\bar{\nu}$	effective cubic coefficient	η^*	parametric coupling coefficient
θ	tether inclination	λ^2	elasto-geometric parameter
C_D	drag coefficient	η_0	non-dimensional pretension
δ	detuning ($\Delta = \varepsilon\delta$)	a	steady vibration amplitude
A	complex slow amplitude	γ	autonomous slow phase
T_0, T_1, T_2	fast, slow, super-slow times	P	response polynomial
F^*	LC1 and LC3 forcing amplitude	$\eta^* a_T$	LC2 parametric pump
Res	resultant	J	slow-flow Jacobian
$\boldsymbol{\theta}$	slow-flow network weights	$\mathcal{G}$	bifurcation-aware operator
h	Mathieu pump depth	$\boldsymbol{\Psi}$	fundamental (monodromy) matrix
$\boldsymbol{d}$	physical design vector	$\mathcal{M}$	design-to-input map
$c(p)$	learned polynomial coefficients	L_c, ω_c	characteristic length, frequency

References

1. Corazza S, Foti F, Martinelli L, et al. Submerged floating tunnels: Nonlinear dynamics of anchoring elements subject to hydrodynamic loads. Journal of Sound and Vibration. 2026; 643: 119981. doi: 10.1016/j.jsv.2026.119981
2. Warnitchai P, Fujino Y, Susumpow T. A non-linear dynamic model for cables and its application to a cable-structure system. Journal of Sound and Vibration. 1995; 187(4): 695–712.
3. Irvine HM. Cable Structures. MIT Press; 1981.
4. Morison JR, Johnson JW, Schaaf SA. The Force Exerted by Surface Waves on Piles. Journal of Petroleum Technology. 1950; 2(5): 149–154.
5. Faltinsen OM. Sea Loads on Ships and Offshore Structures. Cambridge University Press; 1990.
6. Chakrabarti SK. Hydrodynamics of Offshore Structures. Computational Mechanics Publications; 1987.
7. Sarpkaya T. Mechanics of Wave Forces on Offshore Structures. Van Nostrand Reinhold; 1981.
8. Jin C, Kim MH. Time-Domain Hydro-Elastic Analysis of a SFT (Submerged Floating Tunnel) with Mooring Lines under Extreme Wave and Seismic Excitations. Applied Sciences. 2018; 8(12): 2386. doi: 10.3390/app8122386
9. Wang K, Er GK, Iu VP. Nonlinear random vibrations of moored floating structures under seismic and sea wave excitations. Marine Structures. 2019; 65: 75–93. doi: 10.1016/j.marstruc.2018.12.006
10. Cantero D, Rønnquist A, Naess A. Recent Studies of Parametrically Excited Mooring Cables for Submerged Floating Tunnels. Procedia Engineering. 2016; 166: 99–106. doi: 10.1016/j.proeng.2016.11.571
11. Xiong J, Sang S, Du Y, et al. Kinematic Stability Analysis of Anchor Cable Structures in Submerged Floating Tunnel under Combined Parametric–Vortex Excitation. Journal of Marine Science and Engineering. 2024; 12(9): 1478. doi: 10.3390/jmse12091478
12. Mazzolani FM, Landolfo R, Faggiano B, et al. Structural Analyses of the Submerged Floating Tunnel Prototype in Qiandao Lake (PR of China). Advances in Structural Engineering. 2008; 11(4): 439–454. doi: 10.1260/136943308785836862
13. Long X, Ge F, Hong Y. Feasibility study on buoyancy–weight ratios of a submerged floating tunnel prototype subjected to hydrodynamic loads. Acta Mechanica Sinica. 2015; 31(5): 750–761. doi: 10.1007/s10409-015-0428-3
14. Xu W, Ma Y, Liu G, et al. A review of research on tether-type submerged floating tunnels. Applied Ocean Research. 2023; 134: 103525. doi: 10.1016/j.apor.2023.103525
15. Jeong K, Min S, Jang M, et al. Feasibility study of submerged floating tunnels with vertical and inclined combined tethers. Ocean Engineering. 2022; 265: 112587. doi: 10.1016/j.oceaneng.2022.112587
16. Kim S, Kim JG, Jin C, et al. Parametric excitation of submerged floating tunnel caused by nonlinear tether stiffness. Ocean Engineering. 2025; 321: 120327. doi: 10.1016/j.oceaneng.2025.120327
17. Li Y, Yi Z, Wang S, et al. Establishing relations between the vortex-induced vibratory behaviors of tether-type submerged floating tunnel and its multiple intermediate/boundary supporting stiffnesses. Nonlinear Dynamics. 2026; 114(9): 626. doi: 10.1007/s11071-026-12491-y
18. Zhou X, Qiao D, Wang M, et al. Global Dynamic Responses and Progressive Failure of Submerged Floating Tunnel Under Cable Breakage Conditions. China Ocean Engineering. 2024; 38(4): 676–688. doi: 10.1007/s13344-024-0053-7
19. Zhang M, Wang D, Hao Z, et al. Dynamic response predictions of the high-dimensional vortex-induced vibration of the riser with time-varying tension. Nonlinear Dynamics. 2025; 113(12): 14629–14656. doi: 10.1007/s11071-025-10933-7
20. Xie Q, Liu B, Zhang J, et al. Nonlinear Dynamic Response Analysis of Cable–Buoy Structure Under Marine Environment. Journal of Marine Science and Engineering. 2025; 13(1): 176. doi: 10.3390/jmse13010176
21. Yang L, Wang D, Zheng H, et al. Analytical Framework for Tension Characterization in Submerged Anchor Cables via Nonlinear In-Plane Free Vibrations. Journal of Marine Science and Engineering. 2024; 12(8): 1286. doi: 10.3390/jmse12081286
22. Chung WC, Jin C, Kim M, et al. Parametric Study on Mooring System Design of Submerged Floating Tunnel under Extreme Wave and Seismic Excitation. Journal of Marine Science and Engineering. 2023; 11(12): 2357. doi: 10.3390/jmse11122357
23. Nayfeh AH. Perturbation Methods. Wiley-VCH; 2004.
24. Nayfeh AH, Mook DT. Nonlinear Oscillations. Wiley-VCH; 2004.
25. Kevorkian J, Cole JD. Multiple Scale and Singular Perturbation Methods. Springer; 1996.

26. Magnus W, Winkler S. Hill's Equation. Dover; 1979.
27. Kovacic I, Rand R, Mohamed Sah S. Mathieu's Equation and Its Generalizations: Overview of Stability Charts and Their Features. Applied Mechanics Reviews. 2018; 70(2): 020802.
28. Guckenheimer J, Holmes P. Nonlinear Oscillations, Dynamical Systems, and Bifurcations of Vector Fields. Springer; 1983.
29. Golubitsky M, Schaeffer DG. Singularities and Groups in Bifurcation Theory. Springer; 1985.
30. Strogatz SH. Nonlinear Dynamics and Chaos. Westview Press; 2015.
31. Seydel R. Practical Bifurcation and Stability Analysis. Springer; 2010.
32. Zhang C, Li D, Cao F, et al. Multi-scale asymptotic analysis of parametric roll instability for a point-absorber wave energy converter. Nonlinear Dynamics. 2026; 114(6): 395. doi: 10.1007/s11071-026-12275-4
33. Gu XD, Zhang YY, Mughal I, et al. Stochastic responses of nonlinear inclined cables with an attached damper and random excitations. Nonlinear Dynamics. 2024; 112(18): 15969–15986. doi: 10.1007/s11071-024-09877-1
34. Raissi M, Perdikaris P, Karniadakis GE. Physics-informed neural networks: A deep learning framework for solving forward and inverse problems involving nonlinear partial differential equations. Journal of Computational Physics. 2019; 378: 686–707.
35. Karniadakis GE, Kevrekidis IG, Lu L, et al. Physics-informed machine learning. Nature Reviews Physics. 2021; 3(6): 422–440.
36. Krishnapriyan AS, Gholami A, Zhe S, et al. Characterizing possible failure modes in physics-informed neural networks. In: Proceedings of the 35th Conference on Neural Information Processing Systems (NeurIPS 2021); 6–14 December 2021; Sydney, Australia.
37. Wang S, Wang H, Perdikaris P. On the eigenvector bias of Fourier feature networks: From regression to solving multi-scale PDEs with physics-informed neural networks. Computer Methods in Applied Mechanics and Engineering. 2021; 384: 113938.
38. Lu L, Jin P, Pang G, et al. Learning nonlinear operators via DeepONet based on the universal approximation theorem of operators. Nature Machine Intelligence. 2021; 3(3): 218–229.
39. Li Z, Kovachki N, Azizzadenesheli K, et al. Fourier neural operator for parametric partial differential equations. arXiv preprint. 2021; arXiv:2010.08895.
40. Kovachki N, Lanthaler S, Mishra S. On universal approximation and error bounds for Fourier neural operators. Journal of Machine Learning Research. 2021; 22(290): 1–76.
41. Hornik K, Stinchcombe M, White H. Multilayer feedforward networks are universal approximators. Neural Networks. 1989; 2(5): 359–366.
42. Barron AR. Universal approximation bounds for superpositions of a sigmoidal function. IEEE Transactions on Information Theory. 1993; 39(3): 930–945.
43. Brunton SL, Proctor JL, Kutz JN. Discovering governing equations from data by sparse identification of nonlinear dynamical systems. Proceedings of the National Academy of Sciences. 2016; 113(15): 3932–3937.
44. Rudy SH, Brunton SL, Proctor JL, et al. Data-driven discovery of partial differential equations. Science Advances. 2017; 3(4): e1602614.
45. Wan R, Kharazmi E, Triantafyllou MS, et al. DeepVIVONet: Using deep neural operators to optimize the location of sensors with application to vortex-induced vibrations. Journal of Fluids and Structures. 2025; 137: 104330. doi: 10.1016/j.jfluidstructs.2025.104330
46. Dan D, Liao X, Ge L, et al. Physics-Informed Neural Networks for Solving Free Vibration Response of Cables Considering Bending Stiffness. Journal of Vibration Engineering & Technologies. 2025; 13(8): 587. doi: 10.1007/s42417-025-02170-4
47. Chatterjee T, Friswell MI, Adhikari S, et al. MATLAB Implementation of Physics Informed Deep Neural Networks for Forward and Inverse Structural Vibration Problems. Aerospace Research Communications. 2024; 2: 13194.
48. Baniya S, Maity D. A comprehensive review of theoretical concepts and advancements in physics-informed neural networks with applications in structural engineering. Artificial Intelligence Review. 2025; 59(2): 49. doi: 10.1007/s10462-025-11444-y
49. Daneshvar A, Golroo A, Nejad FM, et al. Physics-Informed Neural Networks in Civil, Transportation, and Pavement Engineering: Cross-Domain Review, Benchmarking Challenges, and Research Gaps. Archives of Computational Methods in Engineering. 2026. doi: 10.1007/s11831-026-10643-2
50. Li HWX, Lu L, Cao Q. Motion estimation and system identification of a moored buoy via physics-informed neural network. Applied Ocean Research. 2023; 138: 103677. doi: 10.1016/j.apor.2023.103677

51. Jin C, Hong SH. Underwater Line Monitoring Using Optimally Placed Inclinometers. Journal of Marine Science and Engineering. 2024; 12(11): 1939. doi: 10.3390/jmse12111939
52. Lian J, Ha D, Liang C, et al. Stereo-vision-based mooring tension monitoring method for offshore floating photovoltaic platforms. Mechanical Systems and Signal Processing. 2026; 242: 113686. doi: 10.1016/j.ymssp.2025.113686
53. Luo X, Xie J, Shi W, et al. Internal resonance analysis and parameter optimization of the fractional SD oscillator system. Nonlinear Dynamics. 2025; 113(25): 34843–34869. doi: 10.1007/s11071-025-11848-z
54. Tang Y, Wang G, Ding Q. Nonlinear Fractional-Order Dynamic Stability of Fluid-Conveying Pipes Constituted by the Viscoelastic Materials with Time-Dependent Velocity. Acta Mechanica Solida Sinica. 2022; 35(5): 733–745. doi: 10.1007/s10338-022-00328-1
55. Lian C, Wang J, Jing H, et al. The Analysis of Free Nonlinear Vibrations with Fractional Damping. Journal of Vibration Engineering & Technologies. 2026; 14(1): 37. doi: 10.1007/s42417-025-02251-4
56. Tian Y, Peng X, He J. Frontier advances in solving fractional differential equations via physics-informed neural networks: A comprehensive review. Advances in Differential Equations and Control Processes. 2026; 33(3): 4514. doi: 10.59400/adecp4514

Appendix A. Detailed derivation of the amplitude modulation equations

We record the algebra compressed in Section 4. Starting from the canonical form Equation (7) and the differentiation rule of Definition 5, the substitution of the expansion $z = z_0 + \varepsilon z_1 + \mathcal{O}(\varepsilon^2)$ produces, at successive orders,

$$\mathcal{O}(\varepsilon^0): \quad D_0^2 z_0 + \bar{\omega}^2 z_0 = 0, \tag{A1}$$

$$\mathcal{O}(\varepsilon^1): \quad D_0^2 z_1 + \bar{\omega}^2 z_1 = -2D_0 D_1 z_0 - 2\hat{\xi}\bar{\omega} D_0 z_0 - 3\hat{\beta} z_0^2 - \hat{\nu} z_0^3 + \Xi(T_0, T_1), \tag{A2}$$

where $\hat{\xi} = \hat{\xi}_s + \hat{K}_d a$ and Ξ is the pump $\eta^* a_T \cos(\Omega T_0 + \vartheta) z_0$ for LC2, or the additive drive Φ for LC1 and LC3. The leading solution is Equation (8). Expanding the right-hand side of Equation (A2) in the harmonics of $\bar{\omega}$, only the first harmonic is secular, and its coefficient collects

$$-2\mathrm{i}\bar{\omega} D_1 A, \qquad -2\mathrm{i}\hat{\xi}\bar{\omega}^2 A, \qquad 0, \qquad -3\hat{\nu}\,|A|^2\,A, \tag{A3}$$

the third entry, from the quadratic term, vanishing because z_0^2 carries only the zeroth and second harmonics. To these the drive adds $\frac{1}{2}F^*\,\mathrm{e}^{\mathrm{i}(\bar{\omega}\delta T_1 + \vartheta)}$ for LC1 and LC3, or $\frac{1}{2}\eta^* a_T \bar{A}\,\mathrm{e}^{\mathrm{i}\Phi_T}$ with $\Phi_T = 2\bar{\omega}\delta T_1 + \vartheta$ for LC2.

One calculation serves both conditions. Setting the sum of these contributions to zero, substituting $A = \frac{1}{2}a\,\mathrm{e}^{\mathrm{i}\varphi}$ with $|A|^2 A = \frac{1}{8}a^3 \mathrm{e}^{\mathrm{i}\varphi}$ and $D_1 A = \frac{1}{2}(a' + \mathrm{i}a\varphi')\mathrm{e}^{\mathrm{i}\varphi}$, dividing by $\mathrm{e}^{\mathrm{i}\varphi}$ and introducing the autonomous phase, the imaginary and real parts separate into the modulation equations. For LC1 and LC3 the phase is $\gamma = \bar{\omega}\delta T_1 + \vartheta - \varphi$ and the result is Equation (13); for LC2 it is $\gamma = 2\bar{\omega}\delta T_1 + \vartheta - 2\varphi$ and the result is the pair Equations 10 and 11. Imposing $a' = \gamma' = 0$ and dividing by the positive amplitude isolates the trigonometric functions of the phase,

$$\sin\gamma = \frac{2\bar{\omega}^2(\hat{\xi}_s + \hat{K}_d a)a}{F^*}, \qquad \cos\gamma = \frac{\frac{3}{4}\hat{\nu}a^3 - 2\bar{\omega}^2\delta a}{F^*} \qquad \text{(LC1 and LC3)}, \tag{A4}$$

$$\sin\gamma = \frac{4\bar{\omega}^2(\hat{\xi}_s + \hat{K}_d a)}{\eta^* a_T}, \qquad \cos\gamma = \frac{\frac{3}{2}\hat{\nu}a^2 - 4\bar{\omega}^2\delta}{\eta^* a_T} \qquad \text{(LC2)}. \tag{A5}$$

Squaring and adding each pair, clearing the denominator and expanding $(\hat{\xi}_s + \hat{K}_d a)^2 = \hat{\xi}_s^2 + 2\hat{\xi}_s\hat{K}_d a + \hat{K}_d^2 a^2$ then recovers the sextic Equation (14) from Equation (A4) and the quartic Equation (12) from Equation (A5). It is the cross term $2\hat{\xi}_s\hat{K}_d a$ that produces the odd monomial in each, the algebraic trace of the amplitude-dependent drag. LC3 is LC1 with F^* replaced by the direct forcing $\tilde{f}$. The two response equations differ only in that the pump amplitude occupies the constant term in place of a forcing squared, and that the geometric nonlinearity enters at fourth rather than sixth degree, which records the different resonance order of the two mechanisms.

Remark A1. *The effective cubic coefficient of Remark 1 arises because the quadratic term forces the corrector z_1 at the zeroth and second harmonics, and these components feed back into the first-harmonic balance at second order. Carrying the expansion to $\mathcal{O}(\varepsilon^2)$ and eliminating the corrector reproduces a cubic-type resonant term whose coefficient combines the bare cubic with a negative multiple of the squared quadratic coefficient, giving $\hat{\nu}_e = \hat{\nu} - \kappa\hat{\beta}^2/\bar{\omega}^2$ with a universal positive κ, as in the analysis of Nayfeh and Mook [24].*

Appendix B. Floquet analysis and the Hill determinant

The parametric stability of the trivial state is decided by Equation (15), whose pump depth is the quantity $h = \varepsilon\,\eta^* a_T/\bar{\omega}^2$ introduced in Equation (16) and recovered from the learned coefficients in Proposition 8. Let $\boldsymbol{\Psi}(\tau)$ be the fundamental matrix of the first-order form of Equation (15) with $\boldsymbol{\Psi}(0) = \boldsymbol{I}$, and let $T_p = \pi/[\bar{\omega}(1+\varepsilon\delta)]$ be the pump period. The monodromy matrix is $\boldsymbol{M} = \boldsymbol{\Psi}(T_p)$, and by Definition 7 the trivial state is asymptotically stable when both Floquet multipliers satisfy $|\rho_j| < 1$. Liouville's formula makes the product of the multipliers equal to $\exp(-2\varepsilon\hat{\xi}_s\bar{\omega}T_p)$, so the two cannot both leave the unit disk. The instability boundary is therefore the locus on which the larger multiplier crosses the unit circle, and it is that boundary which is computed in **Figure 14**.

The same boundary can be obtained analytically through the Hill determinant. Seeking a Bloch solution $z = e^{\mu\tau}\sum_{n\in\mathbb{Z}} c_n e^{in\Omega_p\tau}$ with $\Omega_p = 2\bar{\omega}(1+\varepsilon\delta)$ and substituting into Equation (15) gives the three-term recurrence

$$\Big[(\mu + \mathrm{i}n\Omega_p)^2 + 2\varepsilon\hat{\xi}_s\bar{\omega}(\mu + \mathrm{i}n\Omega_p) + \bar{\omega}^2\Big]c_n - \tfrac{1}{2}\bar{\omega}^2 h\,(c_{n-1} + c_{n+1}) = 0, \tag{A6}$$

whose nontrivial solvability is the vanishing of the associated infinite tridiagonal determinant, the Hill determinant $\Delta_H(\mu)$. Because only a single harmonic appears in the pump, the off-diagonal entries are constant and the diagonal entries grow quadratically in n, so the truncated determinant $\Delta_H^{(N)}$ of order $2N+1$ converges to Δ_H geometrically in N. This is the convergence asserted in Proposition 5 and verified numerically in **Figure 24**. At the onset of the principal tongue the solution is subharmonic, carried by the odd multiples of $\bar{\omega}$, and the determinant is real. Retaining only the first harmonic gives the closed form $h^* = 4\varepsilon\hat{\xi}_s$, which is the algebraic boundary of Equation (30) at zero detuning. Each further order contracts the relative deviation from the certified value by about two decades, so three orders suffice to reach the round-off floor, as **Figure 24** records for three damping ratios.

Appendix C. Non-dimensional coefficients and characteristic scales

For reference we record, in **Table A1**, the meaning of the non-dimensional groups of the tether equation Equation (4b), following the reduction of the study by Corazza et al. [1]. The characteristic length and frequency are chosen as the equivalent-horizontal-tether sag and the taut-string frequency respectively, which avoids a singularity for vertical anchoring elements, and the virtual mass per unit length includes the added-mass contribution with a unit added-mass coefficient for a circular section.

Table A1. Non-dimensional groups of the tether equation and their physical role.

Group	Physical role
$\bar{\omega}$	ratio of tether modal frequency to the characteristic frequency
$\bar{\beta}$	strength of the quadratic geometric nonlinearity
$\bar{\nu}$	strength of the cubic geometric nonlinearity
$\bar{\eta}, \bar{\mu}$	support-coupling coefficients entering the parametric term
$\bar{\alpha}, \zeta$	inertial support-coupling coefficients of the additive drive

Table A1. *Cont.*

Group	Physical role
$\bar{K}_d$	drag-induced amplitude-dependent damping group
λ^2	elasto-geometric parameter of Definition 1
η_0	non-dimensional pretension, proportional to the buoyancy-weight ratio

The ordering adopted in Section 4 places the dissipative, nonlinear, forcing and detuning effects at order ε and the parametric coupling coefficient at order unity, and it is the ordering under which the closed forms [1] were obtained. A numerical inspection of the groups for hollow circular sections confirms it. That inspection also finds the coupling coefficients which would transmit the tether response back to the tube to be negligible against the tube static stiffness, and that finding is the basis of Proposition 1.